A wide-area view of the Phoenix dwarf galaxy from Very Large Telescope/FORS imaging

Battaglia, G.; Rejkuba, M.; Tolstoy, E.; Irwin, M. J.; Beccari, G.

Published in:
Monthly Notices of the Royal Astronomical Society

DOI:
10.1111/j.1365-2966.2012.21286.x

Publication date:
2012

Monthly Notices
of the
ROYAL ASTRONOMICAL SOCIETY

Mon. Not. R. Astron. Soc. **424,** 1113–1131 (2012) doi:10.1111/j.1365-2966.2012.21286.x

A wide-area view of the Phoenix dwarf galaxy from Very Large Telescope/FORS imaging⋆

G. Battaglia,[1,2]† M. Rejkuba,[2] E. Tolstoy,[3] M. J. Irwin[4] and G. Beccari[2]

[1]*INAF – Osservatorio Astronomico di Bologna, via Ranzani 1, 40127 Bologna, Italy*
[2]*European Organization for Astronomical Research in the Southern hemisphere, K. Schwarzschild-Str. 2, 85748 Garching, Germany*
[3]*Kapteyn Astronomical Institute, University of Groningen, PO Box 800, 9700 AV Groningen, the Netherlands*
[4]*Institute of Astronomy, Madingley Road, Cambridge CB03 0HA*

Accepted 2012 May 10. Received 2012 April 18; in original form 2012 January 25

ABSTRACT

We present results from a wide-area photometric survey of the Phoenix dwarf galaxy, one of the rare dwarf irregular/dwarf spheroidal transition-type galaxies (dTs) of the Local Group (LG). These objects offer the opportunity to study the existence of possible evolutionary links between the late- and early-type LG dwarf galaxies, since the properties of dTs suggest that they may be dwarf irregulars in the process of transforming into dwarf spheroidals.

Using FORS at the Very Large Telescope (VLT), we have acquired *VI* photometry of Phoenix. The data reach a signal-to-noise ratio (S/N) ~ 10 just below the horizontal branch of the system and consist of a mosaic of images that covers an area of 26×26 arcmin^2 centred on the coordinates of the optical centre of the galaxy.

Examination of the colour–magnitude diagram and luminosity function revealed the presence of a bump above the red clump, consistent with being a red giant branch bump.

The deep photometry combined with the large area covered allows us to put on a secure ground the determination of the overall structural properties of the galaxy and to derive the spatial distribution of stars in different evolutionary phases and age ranges, from 0.1 Gyr to the oldest stars. The best-fitting profile to the overall stellar population is a Sérsic profile of Sérsic radius $R_S = 1.82 \pm 0.06$ arcmin and $m = 0.83 \pm 0.03$.

We confirm that the spatial distribution of stars is found to become more and more centrally concentrated the younger the stellar population, as reported in previous studies. This is similar to the stellar population gradients found for close-by Milky Way dwarf spheroidal galaxies. We quantify such spatial variations by analysing the surface number density profiles of stellar populations in different age ranges; the parameters of the best-fitting profiles are derived, and these can provide useful constraints to models exploring the evolution of dwarf galaxies in terms of their star formation.

The disc-like distribution previously found in the central regions in Phoenix appears to be present mainly among stars younger than 1 Gyr, and absent for the stars $\gtrsim$5 Gyr old, which on the other hand show a regular distribution also in the centre of the galaxy. This argues against a disc–halo structure of the type found in large spirals such as the Milky Way.

Key words: techniques: photometric – galaxies: evolution – galaxies: individual: Phoenix – Local Group – galaxies: stellar content – galaxies: structure.

1 INTRODUCTION

Dwarf galaxies are the most common type of galaxies in the nearby Universe (see e.g. Karachentsev et al. 2004), and are expected to be among the first systems to form in the cosmological context. At larger redshifts galaxies such as those typically seen in the Local Group (LG) cannot be observed. Therefore detailed observations of current properties of LG galaxies offer the opportunity to gain insight into the earliest stages of galaxy formation in the most numerous type of galaxies in the Universe.

LG dwarf galaxies are classified into two main categories: the late-type objects, containing gas and currently forming stars, often have an irregular appearance in the optical and therefore are called dwarf irregulars (dIrrs), while the early-type dwarf spheroidals

⋆Based on FORS observations collected at the European Southern Observatory (ESO), proposal 083.B-0252.

†E-mail: gbattaglia@oabo.inaf.it

(dSphs) – devoid of neutral gas – show a more regular morphology and no current star formation (e.g. Mateo 1998). Dwarf galaxies with intermediate properties – such as no current star formation but containing gas – are called transition types (dTs).

An open question is whether the various types of dwarf galaxies in the LG are intrinsically different objects, or whether they descend from the same progenitors and have evolved through different paths because of environmental and/or internal processes.

The continuum of properties shown by the various types of LG dwarf galaxies (Tolstoy, Hill & Tosi 2009), which makes their classification sometimes uncertain, seems to argue in favour of an evolutionary link. For example, Peg DIG is the most luminous of the few LG transition-type dwarfs (Phoenix, LGS3, DDO210, Leo T and VV 124) and, because of this, it is sometimes considered as a dIrr. For Fornax, which has formed stars until very recently (50–100 Myr ago; Coleman & de Jong 2008) but is now devoid of gas, its classification as a dSph seems to be merely the result of the particular moment in time in which we are observing this galaxy: if we had been able to observe Fornax a few hundred Myr ago, while still forming stars, we would have classified it as a dT or even as a dIrr.

Another hint to a possible evolutionary link is the existence of a 'morphology–density' relation: dIrrs are found at relatively large distances from the large LG spirals [i.e. >300 kpc from the Milky Way (MW)and M31], while the great majority of early-type dwarf galaxies are satellites of the MW or M31, being located at <300 kpc from them. This already suggests that the interaction with the large spirals (hereafter referred to as 'environment') must have played a role in determining the different evolutionary paths of late- and early-type dwarfs. Models based on *N*-body simulations do show that such interactions are a viable explanation to the observed 'morphology–density' relation (e.g. Mayer et al. 2006; Kazantzidis et al. 2011). However, the presence of dSphs (e.g. Cetus and Tucana) and dTs (e.g. Aquarius) at distances such that any strong interaction with either the MW or M31 can be excluded indicates that the environment cannot be the only factor at play but that internal factors (e.g. the depth of the potential well of the single objects) might also play a role.

The lack of knowledge about the detailed properties of dIrrs and dTs hinders the exploration of a possible common origin of LG dwarfs and what might have caused a different evolutionary path.

At a distance of 415 kpc (Hidalgo et al. 2009, hereafter H09), Phoenix is the closest transition-type dwarf, but even basic properties such as its extent are rather uncertain. For example, van de Rydt, Demers & Kunkel (1991, hereafter VDK91) derived an extent of 8.7 arcmin, while Martínez-Delgado, Gallart & Aparicio (1999, hereafter MD99) found a larger value, with a nominal tidal radius of $r_{\rm t} = 15.8^{+4.3}_{-2.8}$ arcmin. Also its heliocentric systemic velocity is under debate: Irwin & Tolstoy (2002) derived a velocity of $-13 \pm 9\,{\rm km\,s^{-1}}$, while Gallart et al. (2001) measured a velocity of $-52 \pm 6\,{\rm km\,s^{-1}}$. Both studies though consider likely an association between Phoenix and the cloud of H I gas found around the galaxy at heliocentric velocity between −30 and $-14\,{\rm km\,s^{-1}}$ (Young et al. 2007).

The star formation history (SFH) of Phoenix has instead been extensively studied (see VDK91; Held, Saviane & Momany 1999; MD99; Holtzman, Smith & Grillmair 2000; Gallart et al. 2004; Menzies et al. 2008; H09). The coexistence of classical Cepheids and anomalous Cepheids and RR Lyrae variables in this system argues for an extended and complex SFH (Gallart et al. 2004). Phoenix has a similar luminosity to the Sculptor dSph ($L_V = 0.9 \times 10^6$ and $2.15 \times 10^6\,{\rm L_\odot}$, respectively; Mateo 1998), and like Sculptor it formed most of its stars more than 10 Gyr ago (H09). However, unlike Sculptor or the majority of other dSphs, it does show recent star formation (MD99), possibly with stars as young as 100 Myr, and there is H I gas associated with the system (Gallart et al. 2001). This means that, unlike the similarly luminous Sculptor, this system was able to retain its gas for the whole of its lifetime, be it because of a larger potential well and/or a less harsh environment, with less stripping and a larger possibility of gas infall with respect to a satellite of the MW.

The most recent study of Phoenix SFH (H09) is based on two *Hubble Space Telescope* pointings that, even if covering a small fraction of the galaxy, reach out to about 4 arcmin from the centre, giving a view of how the SFH changed across the object. The central regions contain stars over a range of ages (from 100 Myr to the oldest stars), while already at 450 pc from the centre 95 per cent of the stars are more than 8 Gyr old. These properties appear to be consistent with the star formation region slowly shrinking with time (H09).

In this paper we investigate the global properties of Phoenix based on wide-area imaging data collected at the European Southern Observatory (ESO) Very Large Telescope (VLT) with FORS. The observations cover a large region, $26 \times 26\,{\rm arcmin^2}$, and reach below the horizontal branch (HB) of the galaxy, containing stars in evolutionary stages representative of the whole age range displayed by Phoenix. This allows us not only to explore the overall structure of the galaxy, but also to directly derive the spatial distribution of stars in different age ranges. The paper is organized as follows: in Section 2 we present the observations and the data reduction procedure adopted; in Section 3 we analyse the overall structure of the galaxy; in Section 4 we use the tip of the red giant branch (RGB) to derive an estimate of the distance modulus to Phoenix; Section 5 deals with the stellar population mix and its spatial variations; we conclude with a discussion in Section 6 and a summary of the results in Section 7.

In a subsequent paper we will complement this photometric study with Ca II triplet (CaT) spectroscopy to investigate the metallicity and internal kinematic properties of this galaxy.

2 OBSERVATIONS AND DATA REDUCTION

The observations were carried out between 2009 June 20 and August 20 in service mode with the ESO VLT instrument FORS2 at UT1 (Antu). FORS2 is a focal reducer multimode instrument that can be used for optical imaging, polarimetry, long-slit and multi-object spectroscopy (Appenzeller & Rupprecht 1992). It has a field of view of $6.8 \times 6.8\,{\rm arcmin^2}$ with pixel size 0.25 arcsec. The detectors are two 2k × 4k MIT CCDs (hereafter referred to as C1 and C2). We used FORS2 in imaging mode to make a mosaic of 4 × 4 fields covering an area of approximately $26 \times 26\,{\rm arcmin^2}$ centred on the coordinates of the optical centre of Phoenix (see Table 1 for the galaxy parameters). One additional field was observed at a displaced location from the galaxy as a check on the determination of the foreground/background density (see Fig. 1). For each pointing we took three dithered exposures of 120 s each in $v_{\rm HIGH}$[1] filter and five dithered exposures of 90 s each in $I_{\rm Bess}$ filter (in the subsequent text, for brevity we denote the filters as V instead of $v_{\rm HIGH}$ and I

[1] This filter has a central wavelength of 555 nm and a full width at half-maximum (FWHM) of 123.2; for the transmission curve see http://www.eso.org/sci/facilities/paranal/instruments/fors/doc/VLT-MAN-ESO-13100-1543_v87.pdf.

Table 1. The various rows are from top to bottom: coordinates of the optical centre; PA, defined as the angle between the northern direction and the major axis of the galaxy measured counter-clockwise; ellipticity, defined as $e = 1 - b/a$; King core and tidal radii; half-light radius, defined as $R_{1/2} \sim 1.68 \times R_e$, where $R_e = 1.37 \pm 0.01$ arcmin is the exponential radius; distance modulus and heliocentric distance; luminosity in V band; V magnitude of the HB; reddening; extinction in V and I bands. The last row quotes the conversion factor from arcmin to kpc at the distance of Phoenix. The PA and ellipticity refer to the outer population, aligned north–south. References: 1 = Mateo (1998); 2 = this work; 3 = Holtzman et al. (2000); 4 = Schlegel, Finkbeiner & Davis (1998), http://irsa.ipac.caltech.edu/applications/DUST/, average value over 2°. The A_V value assumes $A_V/E(B-V) = 3.1$; A_I was derived using the ratio $A_I/A_V = 0.479$ from Cardelli et al. (1989); note that previous works such as H09 assume larger values of reddening, 0.02.

Parameter	Value	Reference	Notes
$(\alpha_{J2000},\delta_{J2000})$	$01^h51^m06^s$, $-44°26'42''$	1	
PA	$8° \pm 4°$	2	Beyond 4.5 arcmin
e	0.3 ± 0.03	2	Beyond 4.5 arcmin
R_{core}	1.79 ± 0.04 arcmin	2	
R_{tidal}	10.56 ± 0.15 arcmin	2	
$R_{1/2}$	2.30 ± 0.07 arcmin	2	
$(m-M)_0$	23.06 ± 0.12	2	
Distance	409 ± 23 kpc	2	
L_V	$0.9 \times 10^6\,L_\odot$	1	Refers to a distance of 445 kpc
V_{HB}	23.9	3	
$E(B-V)$	0.016	4	
A_V	0.050 mag		
A_I	0.024 mag		
1 arcmin kpc^{-1}	0.119		Assuming a distance of 409 kpc

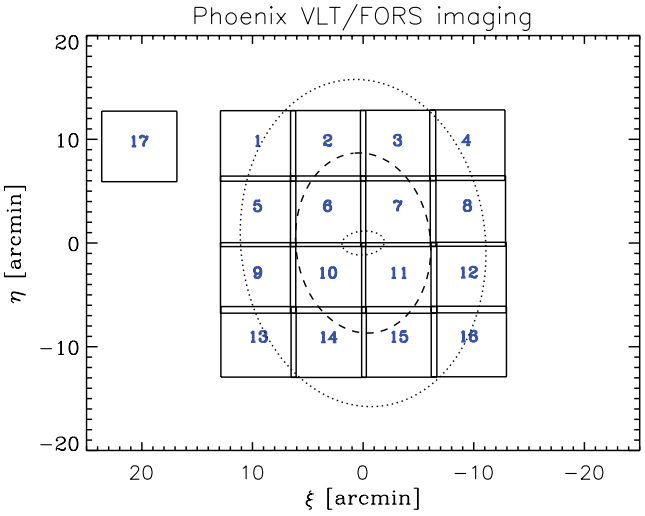

Figure 1. Schematic representation of the coverage of our VLT/FORS photometric data for the Phoenix dwarf galaxy. The black squares indicate the individual pointings, showing the regions of overlap. The inner dotted ellipse (with parameters $e = 0.4$, PA = 95° and semimajor axis = 115 arcsec) denotes the region where the elliptical isopleths show a sharp rotation in their major axes in the analysis of MD99, and where most of the young stars are found. The outer ellipses indicate two measurements for the extent of Phoenix: the dotted one (with parameters $e = 0.3$, PA = 5° and semimajor axis = 15.8 arcmin) shows the nominal tidal radius from the study of MD99, and the dashed one (with parameters $e = 0.3$, PA = 5° and semimajor axis = 8.7 arcmin) where the exponential fit to the surface brightness profile approaches zero from VDK91.

instead of I_{Bess}). The offset sizes between the exposures were such that we covered the gaps between the two detectors. Table 2 lists the observation log of all scientific fields.

As a part of the standard calibration plan for FORS2, observations of standard star fields in these filters were also carried out by ESO service mode observers. The log of all standard star observations is in Table 3.

The basic data reduction steps, consisting of bias subtraction and division by the normalized twilight flat-field exposure, were performed with the ESO FORS imaging pipeline.

For each pointing such pre-reduced images were first aligned to the coordinates of one of the individual exposures, which was acting as the reference image. The regions of the CCD that had no data were masked out – in particular, the so-called slave CCD (bottom CCD) has a large area that gets no light – and the aligned images were then median combined using the IRAF task IMCOMBINE. The image quality was measured on combined images and the FWHM values are given in Table 2. We checked that the FWHM measured on the combined images was similar to those in the individual exposures.

Since the internal regions of Phoenix are relatively crowded, we decided to perform point spread function (PSF) fitting photometry on all of our pointings to get uniform photometry over the whole area. This was done using the stand alone version of the DAOPHOT II package (Stetson 1987).

The routines FIND + PHOTOMETRY + PICK + PSF + ALLSTAR were run separately for each photometric band and for the two FORS CCD chips, accounting for the slightly different readout noise of the CCD chips.

Default parameters were used for the FIND routine to deal with the rejection of bad pixels and elongated objects along the direction of rows and columns. First, objects were located by imposing a 3σ and 4σ threshold above the background on the individual images for the V and I bands, respectively. This threshold value was chosen after inspecting the number of detected objects as a function of threshold parameter, and selecting the value corresponding to the 'knee' where the number of detected objects is changing rapidly with small changes in σ for threshold.

The choice of the PSF stars was done interactively for each field, separately for each filter and each CCD. First, the routine PICK

Table 2. Table of FORS imaging observation for the Phoenix dT. The seeing is the average stellar FWHM from the final, combined, image.

Field name	RA (°)	Dec. (°)	Date and UT of start of observation	Filter	Exptime (s)	Airmass	Seeing (arcsec)
phoenix-img01	27.996042	−44.28881	2009-07-27 9:33:14.097	*V*	3 × 120	1.073	0.60
			9:41:03.332	*I*	5 × 90	1.069	0.60
phoenix-img02	27.848583	−44.28881	2009-07-27 10:00:29.563	*V*	3 × 120	1.062	0.53
			10:08:24.488	*I*	5 × 90	1.062	0.50
phoenix-img03	27.701458	−44.28839	2009-07-28 8:25:56.322	*V*	3 × 120	1.138	0.70
			8:33:59.459	*I*	5 × 90	1.126	0.63
phoenix-img04	27.555667	−44.28756	2009-07-28 8:46:01.520	*V*	3 × 120	1.109	0.67
			8:53:49.835	*I*	5 × 90	1.100	0.63
phoenix-img05	27.99625	−44.39389	2009-07-28 9:05:35.354	*V*	3 × 120	1.091	0.70
			9:13:23.819	*I*	5 × 90	1.084	0.61
phoenix-img06	27.848833	−44.3939	2009-07-24 8:28:10.733	*V*	3 × 120	1.163	0.73
			8:36:03.667	*I*	5 × 90	1.149	0.58
phoenix-img07	27.700833	−44.39395	2009-07-24 8:03:08.061	*V*	3 × 120	1.216	0.63
			8:15:40.713	*I*	5 × 90	1.187	0.56
phoenix-img08	27.554083	−44.39334	2009-07-28 9:30:56.350	*V*	3 × 120	1.071	0.65
			9:38:44.785	*I*	5 × 90	1.068	0.59
phoenix-img09	27.996792	−44.50086	2009-07-28 9:51:22.636	*V*	3 × 120	1.065	0.66
			9:59:12.151	*I*	5 × 90	1.064	0.60
phoenix-img10	27.849125	−44.50111	2009-07-24 8:48:37.538	*V*	3 × 120	1.130	0.66
			8:56:41.984	*I*	5 × 90	1.119	0.60
phoenix-img11	27.69875	−44.50116	2009-06-21 9:35:54.111	*V*	3 × 120	1.324	0.63
			9:43:45.942	*I*	5 × 90	1.298	0.63
phoenix-img12	27.552167	−44.50031	2009-07-29 9:16:05.726	*V*	3 × 120	1.079	0.85
			9:23:58.611	*I*	5 × 90	1.074	0.84
phoenix-img13	27.996333	−44.60359	2009-07-29 9:35:54.979	*V*	3 × 120	1.070	0.73
			9:43:42.634	*I*	5 × 90	1.067	0.69
phoenix-img14	27.847792	−44.6043	2009-07-29 9:56:11.015	*V*	3 × 120	1.064	0.83
			10:04:22.331	*I*	5 × 90	1.064	0.80
phoenix-img15	27.698542	−44.60388	2009-08-20 6:24:45.464	*V*	3 × 120	1.199	0.83
			6:32:43.001	*I*	5 × 90	1.182	0.75
phoenix-img16	27.551292	−44.60303	2009-08-20 6:45:15.295	*V*	3 × 120	1.157	0.86
			6:53:06.891	*I*	5 × 90	1.143	0.80
phoenix-img17	28.246042	−44.28881	2009-08-20 7:05:48.935	*V*	3 × 120	1.126	0.84
			7:13:51.822	*I*	5 × 90	1.115	0.64

was run to automatically select a sample of unsaturated, relatively isolated stars per frame; a PSF was then created, and an image containing the residuals using ALLSTAR. All the PSF stars were then visually examined both on the original image and on the image with subtracted stars. Galaxies, blends or stars with close companions were manually removed from the sample, and the PSF redetermined using this subsample of stars. The procedure was repeated until the only remaining stars to be used for the PSF determination were non-saturated and relatively isolated stars. Typically, between 15 and 30 such stars per frame were used to determine the PSF. We used the option for a spatially non-variable PSF, after testing that no significant differences were introduced by allowing for a spatially variable PSF. The analytical first approximation used as model for the PSF was a Moffat function.

The above procedure, except the creation of the PSFs, was then rerun on the residual images, in order to extract stars that were not previously found due to the wings of brighter stars. We checked that this procedure was not fitting noise by overplotting the position of these fainter stars on top of the image of residuals.

Finally, DAOMATCH and DAOMASTER were used to combine *V* and *I* ALLSTAR PSF fitting photometry of each pointing – separately for the two CCD chips. Only objects detected in both the bands and with magnitude errors <0.5 mag were retained.

Aperture corrections were computed for each field, chip and filter separately using aperture photometry and a curve-of-growth method on a set of well-exposed and isolated PSF stars.

2.1 Astrometry and photometric calibration

The J2000 celestial coordinates of the detected objects were derived with CATAXCORR.[2] The astrometric solution was found by fitting typically a polynomial of third degree between at least 46 stars per pointing and the reference catalogue (USNOA2 and GSC2). The average rms of the solution was 0.2 arcsec in both RA and Dec.

Given that the standard fields used are not crowded, we performed aperture photometry rather than PSF photometry. We located only luminous standard stars by adopting a threshold of 15σ above the background on the individual images.[3] The aperture at which to calculate the instrumental magnitude was derived by examining the run of the magnitude as a function of aperture size for those bright stars that are neither saturated nor close to the border of the image and for which the curve of growth reaches a constant value.

In general an aperture of 25-pixel radius was found to include all the stars' flux for most of the fields of standard stars. However, this

[2] This code was developed by Montegriffo at INAF – Osservatorio Astronomico di Bologna, with the aim of cross-correlating catalogues and finding astrometric solution. The code is routinely used in publications from staff of the INAF – Osservatorio Astronomico di Bologna (e.g. Bellazzini et al. 2011).

[3] We checked that reducing this threshold would significantly increase neither the number of detected stars with catalogued magnitude per frame nor the quality of our calibration.

Table 3. Table of FORS imaging observation for standard fields. The seeing is the average stellar FWHM from the final, combined, image.

Field name	Date and UT of observation	Filter	Airmass	Exptime (s)	Seeing (arcsec)
E5	2009-06-20 22:42:09.728	*V*	1.071	3	0.53
	22:43:39.426	*I*	1.071	1	0.45
E7	2009-07-24 02:02:19.507	*V*	1.067	3	0.80
	02:03:50.096	*I*	1.067	1	1.00
L92	2009-07-27 10:27:40.238	*V*	1.163	3	0.50
	10:29:05.406	*I*	1.165	1	0.53
MarkA	2009-07-27 05:58:03.331	*V*	1.055	3	0.45
	05:59:28.549	*I*	1.056	1	0.43
PG0231_1	2009-07-24 10:23:00.265	*V*	1.176	3	0.65
	10:24:28.883	*I*	1.175	1	0.75
PG0231_2	2009-07-28 10:13:18.350	*V*	1.171	3	0.60
	10:14:43.538	*I*	1.169	1	0.65
PG1525	2009-06-20 22:50:50.644	*V*	1.597	3	0.55
	22:52:19.402	*I*	1.585	1	0.50
PG1657	2009-07-27 00:32:21.166	*V*	1.213	3	0.53
	00:33:46.404	*I*	1.212	1	0.43
PG2213_1	2009-07-27 07:10:52.208	*V*	1.108	3	0.50
	07:12:17.476	*I*	1.109	1	0.48
PG2213_2	2009-07-28 10:22:26.352	*V*	2.015	3	0.73
	10:23:51.520	*I*	2.035	1	0.65
PG2213_3	2009-07-29 06:47:34.819	*V*	1.100	3	0.50
	06:49:00.078	*I*	1.101	1	0.45
PG2213_4	2009-07-29 09:11:13.858	*V*	1.437	3	0.78
	09:12:39.046	*I*	1.445	1	1.00
PG2213_5	2009-07-29 10:29:37.794	*V*	2.181	3	1.50
	10:31:03.072	*I*	2.204	1	0.88
PG2213_6	2009-08-20 07:28:30.579	*V*	1.359	3	0.78
	07:29:09.972	*I*	1.362	1	0.70
T_Phe_1	2009-07-28 09:27:24.530	*V*	1.088	3	0.60
	09:28:49.538	*I*	1.089	1	0.43
T_Phe_2	2009-07-29 10:23:12.828	*V*	1.149	3	0.75
	10:24:38.096	*I*	1.151	1	1.38
T_Phe_3	2009-08-20 07:33:51.860	*V*	1.079	3	0.68
	07:34:30.794	*I*	1.079	1	0.60

aperture radius was too large for a relatively crowded field such as E7; furthermore only a handful of stars passed the above criteria for fields E5 and PG0231: in these three cases we therefore used a smaller aperture radius and derived the aperture correction choosing appropriate isolated stars manually.

Applying the above-described procedure, we extracted 13 standard stars (nine chip1 + four chip2) for the night of June 21; 91 (61+30), 58 (36+22), 19 (11+8) and 28 (19+9) for July 24, 27, 28 and 29, respectively; and 22 standard stars (12+10) for August 20.

We note that the data available for the standard stars are not sufficient to fit simultaneously the zero-point, the extinction coefficient and the colour term for each band, night and chip separately. We therefore follow an iterative approach (Jerjen & Rejkuba 2001), which we apply to the two CCD chips separately.

For each band, we use the equation

$$m_{\rm instr} = M + Z_m + k_m \times X_m + c_m \times (V - I), \quad (1)$$

where $m_{\rm instr}$ and M are the instrumental and calibrated magnitude, X_m the airmass of the pointing, Z_m the zero-point, k_m the extinction coefficient and c_m the colour term. The calibrated photometry for the standard stars was extracted from the online catalogues of Stetson (2000).[4]

On a first pass, we derive the zero-point and extinction coefficient for each night separately by fitting the instrumental magnitudes and keeping the colour term fixed to zero. The derived coefficients are then applied to the calibrated magnitudes of the respective nights, obtaining $m_{\rm step1} = M + Z_{\rm m,fit} + k_{\rm m,fit} \times X_m$; the data of all the nights are then joined together to increase the statistics, and a colour term is fitted to $m_{\rm instr} - m_{\rm step1} = c_{m,\rm fit} \times (V - I) + \text{constant}$. The fitting procedure of the zero-point and extinction term night by night is then repeated, this time by keeping the colour term fixed to $c_{m,\rm fit}$. Any additional dependency on the colour has been added to the colour term.

The average colour term in V band is -0.063 ± 0.012 for C1 and -0.053 ± 0.006 for C2, and is consistent with zero for I band, 0.010 ± 0.006 for C1 and 0.001 ± 0.01 for C2. This compares well with the colour terms available on the ESO quality control webpages for P83,[5] when available for the colour used here. The average extinction term in V band is 0.141 ± 0.015 for C1 and 0.134 ± 0.008 for C2, while in I band it is 0.055 ± 0.011 for C1 and 0.039 ± 0.010 for C2; the determinations for the two chips are consistent with each others within 1σ. The nightly zero-points are listed in

[4] http://www3.cadc-ccda.hia-iha.nrc-cnrc.gc.ca/community/STETSON/standards/

[5] http://www.eso.org/observing/dfo/quality/FORS2/qc/photcoeff/ photcoeffs_fors2.html; note that, as stated on this webpage, the errors on the tabulated quantities are underestimated.

Table 4. Zero-points (ZPs; and their errors) of the photometric calibration transformations (equation 1) derived for each night of observations, separated per band and CCD chip.

Night and CCD chip	ZP *V* band	ZP *I* band
June 21 C1	-27.934 ± 0.025	-27.422 ± 0.043
June 21 C2	-27.997 ± 0.009	-27.400 ± 0.044
July 24 C1	-28.035 ± 0.007	-27.418 ± 0.007
July 24 C2	-28.022 ± 0.007	-27.410 ± 0.011
July 27 C1	-27.956 ± 0.038	-27.485 ± 0.042
July 27 C2	-28.027 ± 0.010	-27.394 ± 0.008
July 28 C1	-28.012 ± 0.030	-27.415 ± 0.027
July 28 C2	-28.049 ± 0.017	-27.373 ± 0.023
July 29 C1	-28.080 ± 0.025	-27.407 ± 0.019
July 29 C2	-28.032 ± 0.026	-27.393 ± 0.033
August 20 C1	-28.005 ± 0.034	-27.378 ± 0.025
August 20 C2	-28.049 ± 0.049	-27.439 ± 0.051

Table 4. The calibrated magnitudes for the science targets were finally derived by iteratively applying the calibration transformations to the instrumental magnitudes to which aperture corrections had been previously applied. The errors on the derived aperture corrections and coefficients of the calibration transformation are included in the error on the calibrated magnitudes.

We used the region of overlap between adjacent fields to place our photometry on a common photometric scale: for this we applied the magnitude shifts derived by comparing the magnitudes of objects in the overlap regions to the various pointings and tied all of them to the system of pointing 06. The applied shifts were typically $<\pm 0.1$ mag; in part the magnitude shifts applied are the consequence of the errors in the calibration of the standard fields, but mostly they arise from the imperfect flat-fielding due to sky concentration in FORS (Freudling et al. 2007).[6] The errors in the determinations of the magnitude shifts were propagated on to the magnitude errors of the individual objects. Obviously pointing 17, which has no overlap with the main mosaic region, could not be placed on the same photometric system. Since, however, we use this pointing only for checks on the determination of the foreground/background density, this will not affect our analysis.

The final step is to merge the catalogues for the various pointings in one catalogue containing a unique set of objects. This is done by performing weighted averages on the observed quantities for stars with multiple measurements.

At this stage we also evaluate which objects we consider as 'stars' on the basis of their PSF fitting shape parameters and errors in magnitudes. Fig. 2 shows the run of the DAOPHOT photometric parameters 'sharpness' and 'χ', as well as the overall magnitude error as a function of the calibrated magnitudes for the sample of unique (combined) measurements. We exclude a priori those objects with relatively large magnitude errors, i.e. $\sigma_V > 0.3$ mag and $\sigma_I > 0.4$ mag. We then examine the distribution of sharpness versus magnitude for this subsample of stars, deriving its scatter per bin of magnitudes. Given the asymmetric distribution around null values of the sharpness parameter, we retain as bona fide stars those objects that fall within the region defined by the exponential envelopes fitted to $+3$ times and -2 times the scatter.[7] The catalogue of bona fide stars consists of 19 286 stars including the control field and 18 919 in the main mosaic area (see Table 5).

Treating photon counts of each star as a Poisson variable, a signal-to-noise ratio (S/N) = 10 would correspond to an error of magnitude of $\sim$0.1 mag and a S/N = 5 to $\sim$0.2 mag. This would imply for this data set a S/N = 10 at the magnitude $V_{10} \sim 24.8$, $I_{10} \sim 23.6$, corresponding to 11 737 stars in the main mosaic area. The magnitude limits at S/N = 5 are $V_5 \sim 25.4$, $I_5 \sim 24.0$. Here we have quoted the shallowest of the values among all fields and chips. The number of stars in the main mosaic area above the S/N = 5 and 10 magnitude limits is 15 238 and 11 737, respectively.

Fig. 3 shows the magnitude differences of the bona fide stars with double measurements. These differences will be used to estimate the typical magnitude and colour error in various magnitude bins (see Section 5.1); in these values are therefore included internal photometric errors, errors from aperture corrections, errors due to the photometric calibration applied to different pointings and effects of crowding (including possible mismatches of stars in the most crowded, inner regions).

In order to understand in more detail the role of crowding in the error budget and on the completeness limit from the inner to the outer parts, we also perform artificial star tests on pointing 06. This is representative of the four central, most crowded pointings (see Fig. 1). Since the FORS field of view is 6.8×6.8 arcmin^2, one single pointing already extents from the centre of Phoenix to about half nominal tidal radius (VDK91; MD99).

We add artificial stars to the combined *V* and *I* images for C1 and C2 separately, using the PSF model derived for pointing 06. The coordinates and magnitudes are randomly chosen from a uniform distribution, and cover the whole extent of the pointing and instrumental magnitudes of stars in Phoenix (corresponding to calibrated magnitude in the ranges *V* [20,27] and *I* [18.5,26.5]). We inject 200 artificial stars per band per chip (about 5–10 per cent of the observed number of stars in these chips), and repeat the experiment five times. Finally, we apply the same reduction and selection procedure that we used to produce the final catalogue of stars. We find that crowding does not significantly affect the 50 per cent completeness limit (i.e. the magnitude at which the fraction of recovered versus injected number of stars is 0.5): in *I* band this is found to be constant around $I \sim 23.5$–23.8 over the explored range of *R*, while in *V* it is $V \sim 24.2$ in the inner 1.5 arcmin, and at larger *R* it remains constant at $V \sim 25$. These values are very similar to the S/N = 10 limits quoted above.

The difference of recovered and input magnitudes of the artificial stars as a function of recovered magnitude is fairly symmetric around zero, showing that – except for a handful of stars – blending is not affecting the recovered magnitudes. The scaled m.a.d. between the difference of input and recovered calibrated magnitude is smaller than those determined using the stars from double measurements, e.g. in the most crowded region it is 0.07 mag for *V* between 24 and 25, and 0.09 mag for *V* between 23 and 24. The errors from Fig. 3, which we use throughout the analysis, can then be considered as conservative.

[6] Although the report from Freudling et al. described in detail the photometric accuracy of FORS1, it is expected that FORS2 flat-fields present similar effects as the two cameras have the same optics and differ only in the detector type.

[7] The scatter is derived in an iterative manner and it is the scaled median absolute deviation (m.a.d.) of the sharpness per magnitude bin of 0.5 mag.

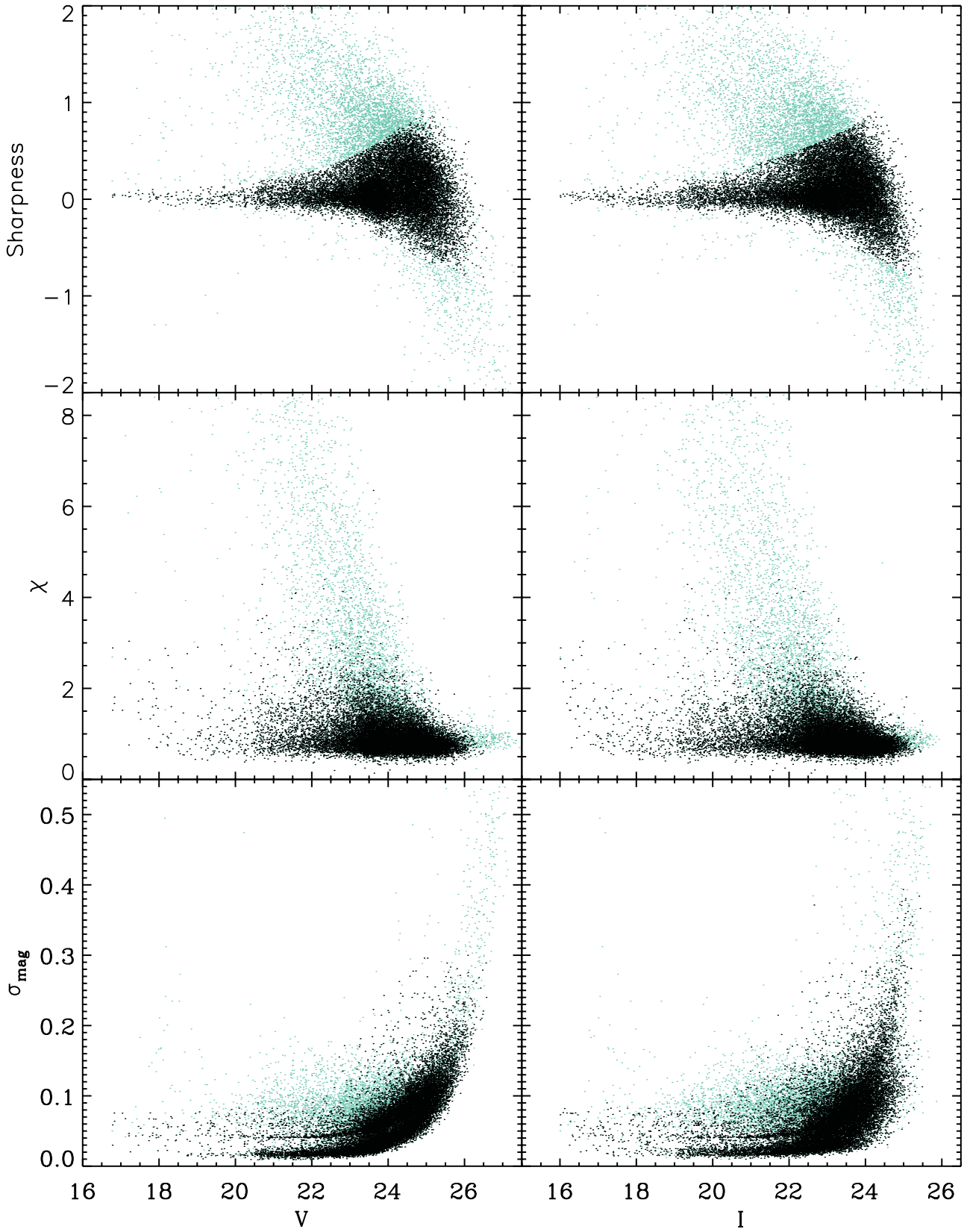

Figure 2. Photometric parameters for the detected sources (cyan points) as a function of the calibrated V magnitude (left) and I magnitude (right). The top and central panels show the sharpness and χ parameters, respectively, from DAOPHOT. The bottom panels show the photometric errors. Besides the magnitude error output from DAOPHOT, these errors factor in the uncertainties from PSF correction, photometric calibration and the shifts applied to the individual magnitudes so as to bring all the photometry to the system of pointing 6. The black points show only those sources which we consider as 'stars' on the basis of their sharpness parameter, and that have $\sigma_V < 0.3$ mag and $\sigma_I < 0.4$ mag.

Table 5. Catalogue of bona fide stars from FORS photometry of the Phoenix dT, including pointing 17. Columns are as follows: (1) the names of the stars; (2) RA in degrees; (3) Dec. in degrees; (4) V magnitude; (5) error in V magnitude; (6) I magnitude; (7) error in I magnitude; (8) χ; (9) and sharpness. This is a sample of the full table, which is available as Supporting Information with the online version of the article.

Name	RA (°)	Dec. (°)	V	σ_V	I	σ_I	χ	Sharpness
phx00001	27.9264897	−44.2962170	25.0495	0.1396	23.8995	0.1396	1.2195	0.6250
phx00002	28.0484214	−44.2960092	25.4608	0.1679	23.8604	0.1679	1.1445	0.6710
phx00003	28.0380659	−44.2959729	25.3526	0.0983	22.8875	0.0983	0.7605	0.2435
phx00004	28.0376092	−44.2955426	24.8144	0.0926	24.5143	0.0926	0.6230	0.2570
phx00005	28.0383987	−44.2954079	25.3673	0.1125	23.0559	0.1125	0.7450	0.1105
phx00006	27.9966041	−44.2952897	24.2082	0.0921	23.2352	0.0921	1.4590	0.5680
phx00007	27.9471308	−44.2953097	24.5857	0.0768	24.0239	0.0768	0.7310	0.1025
phx00008	28.0220882	−44.2952300	25.6432	0.1224	23.3985	0.1224	0.9160	0.4125
phx00009	27.9638667	−44.2951593	24.3899	0.0847	23.6765	0.0847	0.9075	0.3655
phx00010	28.0697991	−44.2950072	24.5369	0.0996	23.6116	0.0996	1.2930	0.5940

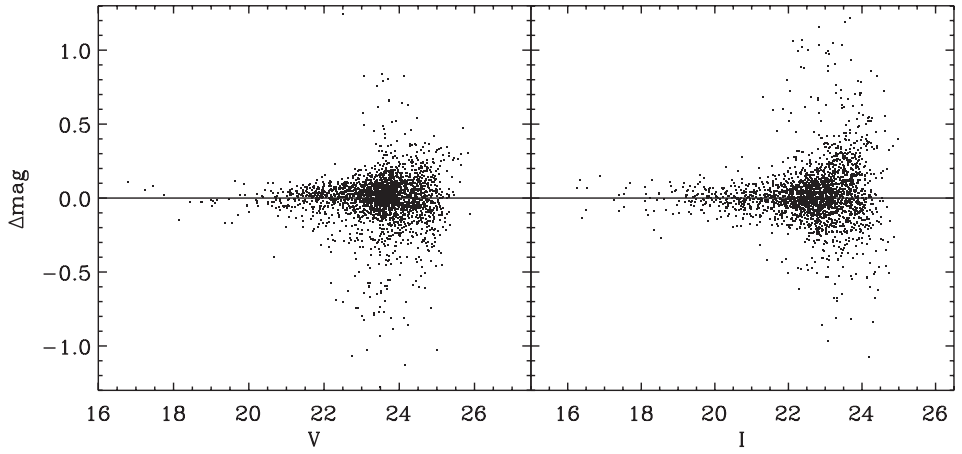

Figure 3. Magnitude difference for stars in the overlapping regions between different pointings and with double measurements as a function of calibrated magnitudes (left: V band; right: I band). Here we plot only the stars that passed the selection criteria in sharpness and photometric errors (see Fig. 2). The scaled m.a.d. at the bright end side of the distribution is 0.054 mag for the V band ($19 < V < 21$) and 0.065 mag for the I band ($18 < I < 20$), corresponding to errors in the individual measurements of 0.038 and 0.046 mag. At the faint end side these numbers are 0.14 and 0.13 mag ($24 < V < 25$ and $23 < I < 24$, respectively), corresponding to errors in the individual measurements of 0.1 and 0.09 mag. At the bright end the photometric errors are 0.033 and 0.035 mag for V and I bands, respectively, and at the faint end they are 0.076 and 0.069 mag. Therefore, the magnitude differences from stars with multiple measurements are inflated by extra 0.01 and 0.03 mag, and at the faint end by 0.06 and 0.06 mag.

3 THE OVERALL STRUCTURE OF PHOENIX

3.1 2D distribution

When analysing the 2D distribution of stars in Phoenix, MD99 found a sharp variation in the trend of the ellipticity ($e = 1 - b/a$, where b and a are the minor and major axes of the ellipse) and position angle (PA) of the isopleths with radius, with e changing from 0.4 to 0.3 and the PA from 95° to 5° around 115 arcsec. The authors noted that the majority of young stars were contained in the flattened central 'component' tilted with respect to the main body of the galaxy and the authors proposed this may be a disc–halo structure, as for large spiral galaxies.

We construct Hess diagrams of the spatial distribution of Phoenix stars, using the sample at S/N > 5 and 10 (brighter than $V_5 \sim 25.4$, $I_5 \sim 24.0$, and than $V_{10} \sim 24.8$, $I_{10} \sim 23.6$, respectively), in bins of 0.3 arcmin. Since in some parts there appear to be voids or enhancements in the stellar number counts with respect to the surroundings, e.g. in the overlap region between pointings, we prefer not to smooth the spatial distribution because this may enhance such features. Fig. 4 shows the resulting distribution for the S/N > 10 sample: it is clearly visible that the inner parts display a different distribution than the outer parts, being almost perpendicular to each other.

We run the IRAF task ELLIPSE on the above Hess diagrams, letting the centre, e and PA of the isophotes at different radii to be free parameters. The results are shown in Fig. 5 for the S/N > 10 sample: within a radius of 1 and 2 arcmin, the centre appears to be located about 0.6–0.2 arcmin east and 0.1 arcmin south from the value listed in Mateo (1998); the ellipticity decreases from a value of 0.44 ± 0.05 at 1 arcmin to 0.1 at about 3 arcmin, to increase again, with an average value of 0.28 ± 0.03 at $R \geq 4.5$ arcmin; the PA varies from about 80° within 2 arcmin and decreases, reaching an average value of $8° \pm 4°$ at $R \geq 4.5$ arcmin. These results are very similar to those resulting from the S/N> 5 sample. They are also in good agreement with those of MD99, even though their results on the 2D distribution may have been more affected by crowding because of the larger seeing of the observations. We discuss the possibility of this being a disc–halo structure in Section 5.

The intermediate values of ellipticity and PA that can be seen around 2 arcmin are probably due to the superposition of the inner and outer components.

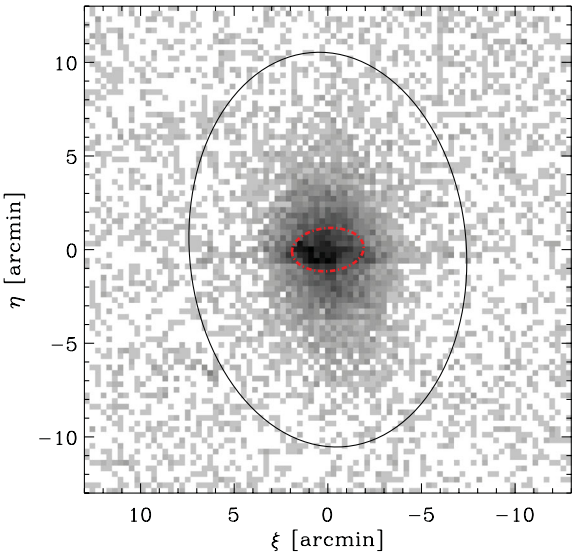

Figure 4. Hess diagram in bins of 0.3 arcmin of the spatial distribution of the stars down to $V = 24.8$ and $I = 23.6$ (S/N> 10). The solid ellipse shows the nominal tidal radius derived in this work, $r_t = 10.56 \pm 0.15$ arcmin ($e = 0.3$ and PA $= 5^\circ$); for the inner dot–dashed ellipse see the caption of Fig. 1.

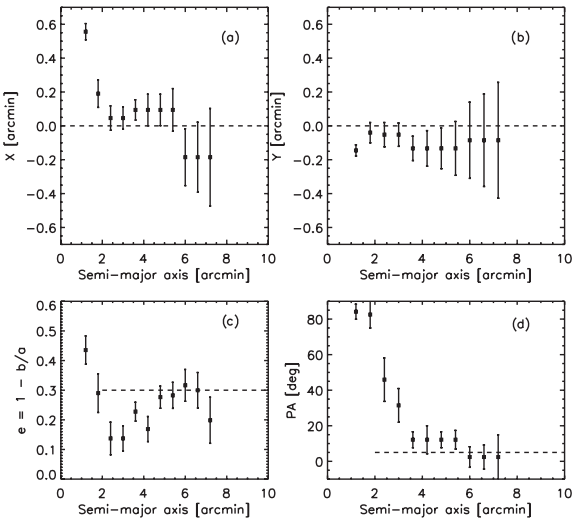

Figure 5. The variation with projected radius of the central position [x and y coordinates, (a) and (b), respectively], (c) ellipticity and (d) PA for the entire stellar population of Phoenix, for the stars brighter than $V = 24.8$ and $I = 23.6$ (S/N > 10) from our FORS imaging data. The variation of the central position is with respect to the value listed in Mateo (1998). The horizontal lines in panels c) and d) indicate the values of the ellipticity and PA found for the outer Phoenix population by MD99.

3.2 Surface number density profile

There have been previous determinations of the surface number density profile of Phoenix, with results rather different from each other: VDK91 used a scanned ESO/SRC IIIaL plate and found that the surface brightness profile is not well fitted by a King profile but decreases exponentially, reaching the zero level at 8.7 arcmin from the centre; on the other hand, MD99 find that the profile can be well fitted by a King profile, and determine a nominal tidal radius of $r_t = 15.8^{+4.3}_{-2.8}$ arcmin.

We derive the surface number density profile of the overall stellar population of Phoenix using both the data sets with S/N > 5 and 10. We sample the number counts in elliptical bins.[8] For the values of ellipticity of the elliptical bins we adopt the values for the outer components of MD99, i.e. $e = 0.3$ and PA $= 5^\circ$, given the good agreement between our results and those of MD99, and the fact that MD99 derived those parameters from a single plate rather than a mosaic of images.

Table 6. Values of the density of contaminants (number arcmin^{-2}) as derived from the weighted mean of the outer points of the surface number density profile of the various populations (column 2), from the objects at elliptical radii >12.6 arcmin (column 3) and from pointing 17 (column 4). Note that since the MS stars display an asymmetric distribution, we do not derive surface number profiles for them. For those populations that have stars as faint as the V_5, I_5 magnitude, we perform two determinations: one considering the stars brighter than the V_{10}, I_{10} limit (labelled as 10) and those brighter than the V_5, I_5 one (labelled as 5). Note that the majority of the determinations are compatible within 1σ between the three methods.

	Weighted mean	$R > 12.6$ arcmin	Field 17
MS	–	0.012 ± 0.006	0.022 ± 0.022
MS 10	–	0.0	0.022 ± 0.022
BL	0.11 ± 0.02	0.092 ± 0.017	0.087 ± 0.04
RC	0.543 ± 0.055	0.474 ± 0.038	0.281 ± 0.078
AGB bump	0.056 ± 0.018	0.037 ± 0.011	0.065 ± 0.037
RHB	0.338 ± 0.046	0.361 ± 0.033	0.238 ± 0.072
BHB 5	0.07 ± 0.023	0.092 ± 0.017	0.043 ± 0.031
BHB 10	0.053 ± 0.020	0.049 ± 0.012	0.022 ± 0.022
RGB	0.055 ± 0.020	0.046 ± 0.012	0.022 ± 0.022
All 5	8.44 ± 0.24	8.15 ± 0.16	7.40 ± 0.40
All 10	5.52 ± 0.19	5.35 ± 0.13	5.58 ± 0.35

Given the discrepant measurements of the extent of Phoenix in the literature, we decided to estimate empirically the density of contaminant objects (MW foreground stars and unresolved galaxies), rather than relying on uncertain selection of a region supposedly free of Phoenix stars. The following two approaches were adopted: (a) we compute the number density profile in elliptical annuli whose semimajor axis is $\lesssim$13 arcmin, i.e. the whole ellipse is contained in our main mosaic area; we analyse the outer parts of the profile, and adopt as density of contaminants a weighted average of the outer points, where the profile becomes approximately flat; in this case this is the outermost 3 arcmin; (b) we analyse the number density profile along the projected minor axis of the galaxy; this is because in that direction our mosaic covers a region corresponding to rather large elliptical radii, 18.6 arcmin, i.e. a region beyond the largest literature measurement of the nominal tidal radius of the galaxy (15.8 arcmin; MD99); along this axis, we find that the profile flattens at ∼8.8 arcmin, corresponding to an elliptical radius of 12.6 arcmin; we therefore expect the great majority of the objects found at elliptical radii larger than 12.6 arcmin to be composed of contaminants; we then use the objects located at elliptical radius >12.6 arcmin to determine the density of contaminants. The values we obtain with the two methods are consistent with each other (see Table 6). As a consistency check, we compare these determinations to the ones derived from pointing 17 (see Table 6), i.e. the pointing displaced from the rest of the mosaic area, and also find good

[8] Throughout the manuscript the projected elliptical radius of a point (x, y) is defined as $R = \sqrt{x^2 + y^2/(1-e)^2}$, where e is the considered ellipticity, and the galaxy is assumed to be centred on the origin, with its major axis aligned with the x-axis.

agreement; however, given the small area covered by pointing 17, we will be using the other two methods in the following analysis.

We subtract the density of contaminants derived from methods (a) and (b) from the number density profile of Phoenix sampled in bins of 0.5 arcmin, and we fit this contamination-subtracted profile to several surface brightness models using a least-squares fit to the data. We used an empirical King profile (King 1962), an exponential profile, a Sérsic profile (Sersic 1968) and a Plummer model (Plummer 1911).

The King model has been extensively used to describe the surface density profile of dSphs:

$$I_{\rm K}(R) = I_{0,\rm K}\left(\frac{1}{\sqrt{1+\left(\frac{R}{r_{\rm c}}\right)^2}} - \frac{1}{\sqrt{1+\left(\frac{r_{\rm t}}{r_{\rm c}}\right)^2}}\right)^2. \quad (2)$$

It is defined by three parameters: a characteristic surface density, $I_{0,\rm K}$, core radius, $r_{\rm c}$, and tidal truncation radius, $r_{\rm t}$.

We note that excesses of stars have been found beyond the King tidal radius in Fornax (e.g. Coleman et al. 2005a; Battaglia et al. 2006), Sculptor (e.g. Coleman, Da Costa & Bland-Hawthorn 2005b; Battaglia et al. 2008) and in a number of other LG dSphs, e.g. Carina (Majewski et al. 2005), Draco (e.g. Wilkinson et al. 2004) and Ursa Minor (e.g. Irwin & Hatzidimitriou 1995; Martínez-Delgado et al. 2001). Since the tidal radius is set by the tidal field of the host galaxy, the observed excesses of stars have been interpreted as tidally stripped stars. However, if dwarf galaxies are embedded in massive dark matter haloes, this tidal radius loses its meaning of tidal truncation radius (we will therefore refer to it as 'nominal tidal radius') and such excesses of stars need not be tidally stripped stars but can simply be due to the King model not providing the best representation of the surface number count profiles of dSphs at large radii.

The Sérsic profile is known to provide a good empirical formula to fit the projected light distribution of elliptical galaxies and the bulges of spiral galaxies (e.g. Caon, Capaccioli & D'Onofrio 1993; Caldwell 1999; Graham & Guzmán 2003; Trujillo et al. 2004); it also provides a good representation of the surface number density of some dSphs (e.g. Battaglia et al. 2006, 2008):

$$I_{\rm S}(R) = I_{0,\rm S}\exp\left[-\left(\frac{R}{R_{\rm S}}\right)^{1/m}\right], \quad (3)$$

where $I_{0,\rm S}$ is a scale surface density, $R_{\rm S}$ is a scale radius and m is the surface density profile shape parameter.

We find that the best-fitting parameters are very similar when using the contaminant density derived from either method (a) or method (b). In the following we will adopt method (a) because the fits to the surface brightness profile produce slightly better χ^2 values; method (a) will be replaced by method (b) only when analysing the young main-sequence (MS) stars because of their asymmetric distribution (see Section 5.2).

The results of the fit for the S/N > 10 sample are shown in Fig. 6 and summarized in Table 7. In our analysis, the Sérsic profile is the one that fits the data best, yielding a reduced $\chi^2 = 1.8$ for a scale radius $R_{\rm S} = 1.82 \pm 0.06$ arcmin and $m = 0.83 \pm 0.03$. An exponential profile with exponential radius 1.37 ± 0.01 arcmin (reduced $\chi^2 = 3.2$) and a King profile with core radius $r_{\rm c} = 1.79 \pm 0.04$ arcmin and tidal radius $r_{\rm t} = 10.56 \pm 0.15$ arcmin (reduced $\chi^2 = 3.5$) also reproduce the data rather well; the Plummer profile instead clearly overpredicts the surface number density at $R \gtrsim 7$ arcmin. The results from the S/N >5 sample are very similar, both in terms

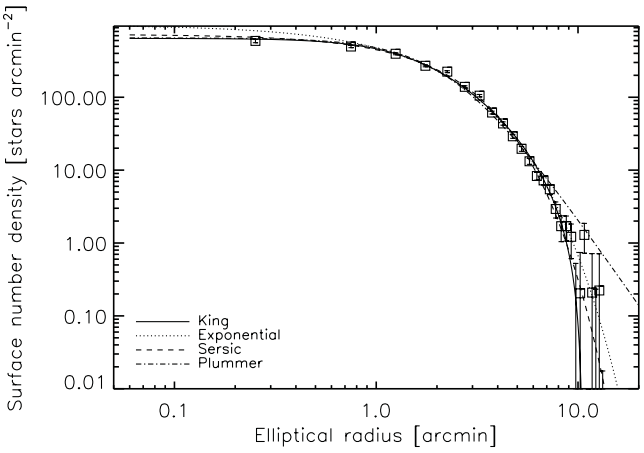

Figure 6. The surface number density profile for the Phoenix dwarf galaxy with overlaid best-fitting King, Sérsic, exponential and Plummer models (solid, dashed, dotted, dot–dashed lines, respectively). The density of contaminants, 5.52 ± 0.19 stars arcmin^{-2} calculated from a weighted average of the outer 3 arcmin, has been subtracted from each point. The error bars are obtained by summing in quadrature the errors from Poisson statistics and the error in contamination. The central point was excluded from the fit. Our best fit to the data is a Sérsic profile with Sérsic radius, $R_{\rm S} = 1.82 \pm 0.06$ arcmin and $m = 0.83 \pm 0.03$ with a reduced $\chi^2 = 1.8$; a King profile with core radius $r_{\rm c} = 1.79 \pm 0.04$ arcmin and tidal radius $r_{\rm t} = 10.56 \pm 0.15$ arcmin gives a reduced $\chi^2 = 3.5$. The best-fitting parameters for the different models are summarized in Table 7.

of shape parameters and best-fitting profiles. Because of the intrinsic uncertainty in determination of crowding corrections and because we are mostly interested in the large-scale properties of Phoenix, we are not applying a crowding correction factor. Instead, we have performed the fit excluding the central point of the surface number count profile. It was anyway shown in Section 2.1 that the effects of crowding are not significant. This is confirmed by the results of the fit to the surface number count profile derived from the sample of stars brighter than the 50 per cent completeness limit at $R < 1.5$ arcmin: the best-fitting parameters are in very good agreement with those derived from the sample S/N > 10, and they yield very similar χ^2 values.

In order to assess whether Sérsic and King profiles perform better because of one more free parameter when compared to exponential and Plummer profiles, we check how the performance of the best-fitting profiles would be ranked using the Akaike information criterion (Akaike 1973) in the form $\chi^2 + 2 \times k$, where k is the number of free parameters in the fit: the ranking of the best-fitting profiles remains the same as according to the reduced χ^2 values; therefore hereafter we consider only the reduced χ^2 values.

Our determination of the tidal radius $r_{\rm t} = 10.56 \pm 0.15$ arcmin is smaller than the one from MD99, $r_{\rm t} = 15.8^{+4.3}_{-2.8}$ arcmin; note that the value from MD99 was derived using the surface number density between projected radii of approximately 2 and 5 arcmin, and extrapolating the behaviour at larger distances, while our determinations come from a much wider area.

Since the outer parts of the object are almost equally well fitted by a range of profiles, continuous and truncated, it is therefore difficult to establish whether Phoenix was tidally truncated by the MW or not.

In the following we will use the King tidal radius we obtained as an indication of the extent of Phoenix, and we will refer to it as the 'nominal' tidal radius as it is unclear whether this is the radius of tidal truncation of the galaxy.

Table 7. Parameters of the best-fitting King model (core radius, r_c, and tidal radius, r_t), Sérsic model (Sérsic radius, R_S, and shape parameter, m), exponential model (scale radius, $r_{Ex,h}$) and Plummer model (scale radius, b) for various stellar populations in Phoenix dSph. For each model we list the corresponding reduced χ^2, $\chi^2_{red} = \chi^2/(N-\nu)$, where N is the number of points in the surface number count profile and ν the number of degrees of freedom. The errors in the parameters are from Monte Carlo simulations but agree well with the formal errors from the fitting procedure. These values of the parameters were derived by using the density of contaminants from the weighted average of the last points of the surface number profile. The best-fitting profiles have good values of the reduced χ^2.

	King			Sérsic			Exponential		Plummer	
	r_c (arcmin)	r_t (arcmin)	χ^2_{red}	R_S (arcmin)	m	χ^2_{red}	$r_{Ex,h}$ (arcmin)	χ^2_{red}	b (arcmin)	χ^2_{red}
All 5	1.82 ± 0.04	10.77 ± 0.17	3.0	1.76 ± 0.07	0.86 ± 0.03	2.0	1.40 ± 0.01	2.9	2.50 ± 0.02	6.7
All 10	1.79 ± 0.04	10.56 ± 0.15	3.5	1.82 ± 0.06	0.83 ± 0.03	1.8	1.37 ± 0.01	3.2	2.43 ± 0.02	7.9
BL	0.73 ± 0.13	9.53 ± 0.70	1.0	0.53 ± 0.26	1.25 ± 0.24	0.9	0.86 ± 0.05	0.9	1.47 ± 0.09	0.9
RC (23.2–23.4)	1.11 ± 0.09	9.98 ± 0.32	1.9	1.45 ± 0.27	0.82 ± 0.11	1.1	1.05 ± 0.04	1.2	1.79 ± 0.06	1.9
RC (23.4–23.6)	1.37 ± 0.08	10.40 ± 0.25	2.4	2.10 ± 0.26	0.66 ± 0.08	0.8	1.17 ± 0.03	1.5	2.00 ± 0.06	3.0
RC (23.6–23.8)	1.91 ± 0.09	10.66 ± 0.23	2.0	2.54 ± 0.23	0.62 ± 0.07	1.1	1.37 ± 0.03	2.1	2.36 ± 0.06	3.7
RGB bump	1.81 ± 0.13	11.08 ± 0.38	0.9	1.88 ± 0.24	0.83 ± 0.08	0.9	1.39 ± 0.04	1.0	2.34 ± 0.06	2.2
RHB	2.40 ± 0.13	10.42 ± 0.18	2.2	2.85 ± 0.19	0.61 ± 0.04	1.9	1.48 ± 0.03	3.5	2.57 ± 0.04	5.8
BHB 10	2.68 ± 0.33	10.72 ± 0.61	1.3	2.87 ± 0.47	0.65 ± 0.10	1.2	1.63 ± 0.07	1.5	2.89 ± 0.15	1.8
BHB 5	2.15 ± 0.30	12.05 ± 0.75	0.7	1.91 ± 0.36	0.91 ± 0.08	0.9	1.61 ± 0.06	0.9	2.70 ± 0.12	1.8
RC	1.77 ± 0.04	10.28 ± 0.12	4.6	2.24 ± 0.11	0.68 ± 0.03	1.6	1.31 ± 0.02	4.2	2.28 ± 0.03	9.1
RGB	1.75 ± 0.07	10.66 ± 0.18	2.3	2.18 ± 0.19	0.71 ± 0.05	0.7	1.33 ± 0.03	1.7	2.25 ± 0.05	4.6

4 TIP OF THE RGB

We derive the tip of the RGB of Phoenix in I-band, I_{RGBT}, and compare it to the determinations from previous works. In addition to providing an independent distance determination, this also offers a possibility to check our photometric calibration.

For this, we convolve the luminosity function (LF) in the I band for stars with $18 < I < 21$ with a Sobel edge-detection kernel [−2,0,2] (Lee, Freedman & Madore 1993), which gives a maximum where the discontinuity in the LF is greatest (see Fig. 7, left).

In order to factor in the uncertainties due to the binning of the LF, we perform the determination over 100 random realizations of the luminosity range used for the calculation – that is, we allow the brightest end of the range to vary between $I = 18$ and 19, and the faintest end between 21 and 22. For each of these random realizations, we perform the convolution using bin sizes decreasing from 0.15 to 0.05 mag with step of 0.01 mag. Since there are several discontinuities in the LF due to various features in the colour–magnitude diagram (CMD; see below), we restrict our search for the maximum to the region $18 < I < 20$; this choice comes from an educated guess from a visual inspection of the CMD and from the literature values of I_{RGBT}.

We find $I_{RGBT} = 19.08 \pm 0.06$, where the error is the scaled m.a.d. of the distribution of values. This agrees with previous measurements such as those by H09, who find $I_{RGBT} = 19.14 \pm 0.02$, and MD99, $I_{RGBT} = 19.00 \pm 0.07$ mag. These authors use a slightly different version of the Sobel filter, i.e. with a kernel [1,2,0,−2,−1], but we checked that the use of this kernel makes no difference to our determination.

We adopt a reddening value $E(B-V) = 0.016$ (see Table 1) derived from the reddening maps of our Galaxy available at http://irsa.ipac.caltech.edu/applications/DUST/ centred on the coordinates of the Phoenix dwarf galaxy. This corresponds to an extinction in V band of $A_V = 0.05$ mag and that in I band of $A_I = 0.024$ (Cardelli, Clayton & Mathis 1989), yielding a dereddened magnitude for the RGB tip $I_{RGBT0} \sim 19.06$.

As shown in Lee et al. (1993) the absolute magnitude of the tip of the RGB in I band changes by less than 0.1 mag around the value $M_I = -4.0$ in the metallicity range $-2.2 <$ [Fe/H] < -0.7, which includes the metallicity range expected for stars in Phoenix (see H09). Therefore by adopting an absolute magnitude $M_{I,RGBT} = -4.0$ and an extinction $A_I = 0.024$, a $I_{RGBT} = 19.08$ would give a distance modulus $(m-M)_0 = 23.06 \pm 0.12$; the error is due to the combination of the estimated error on the determination of I_{RGBT} and the fact that we are neglecting the (weak) dependence of the absolute magnitude of the RGB tip in I band on [Fe/H] (i.e. the 0.1-mag variation of the magnitude of the tip around the value $M_I = -4.0$ mentioned above). This is in good agreement with the value from H09. The distance inferred from this distance modulus is 409 ± 23 kpc.

If we take explicitly into account the dependence of $M_{I,RGBT}$ on global metallicity [M/H], using the calibration from Bellazzini et al. (2004), we would obtain a distance modulus $(m-M)_0 = 23.07$ and 23.12 for $[\alpha/Fe] = 0.0$ and $= +0.4$, respectively, fully compatible with the determination above. Here we made use of the formulae from Salaris, Chieffi & Straniero (1993), [M/H] = [Fe/H] + alog10($0.638 \times 10^{[\alpha/Fe]} + 0.362$) , and Da Costa & Armandroff (1990), $[Fe/H] = -15.16 + 17.0 \times (V-I)_{0,-3} - 4.9 \times (V-I)^2_{0,-3}$, where $(V-I)_{0,-3}$ is the mean colour of the RGB at an absolute I magnitude of -3 that for our data is $(V-I)_{0,-3} = 1.21$.

5 STELLAR POPULATIONS IN PHOENIX AND THEIR SPATIAL VARIATIONS

5.1 Stellar populations in the colour–magnitude diagram

Fig. 8 shows the resulting CMD for our FORS mosaic of the Phoenix dwarf galaxy (left: V band; right: I band; lines of $V_{10} \sim 24.8$, $I_{10} \sim 23.6$ and $V_5 \sim 25.4$, $I_5 \sim 24.0$ are plotted in the figure). The main features of the stellar population of Phoenix are clearly visible and indicated with boxes on the CMD: a well-defined RGB, which should also contain a component of asymptotic giant branch (AGB) stars; a clear detection of a HB, divided into a red (RHB) part and a blue (BHB) part, extending to $V - I \sim 0$; a well-populated red clump (RC); an approximately vertical sequence of young MS stars, centred at $V - I \sim -0.2$; a vertical sequence of stars emerging from the RC, at $V - I \sim 0.7$, containing blue loop (BL) stars.

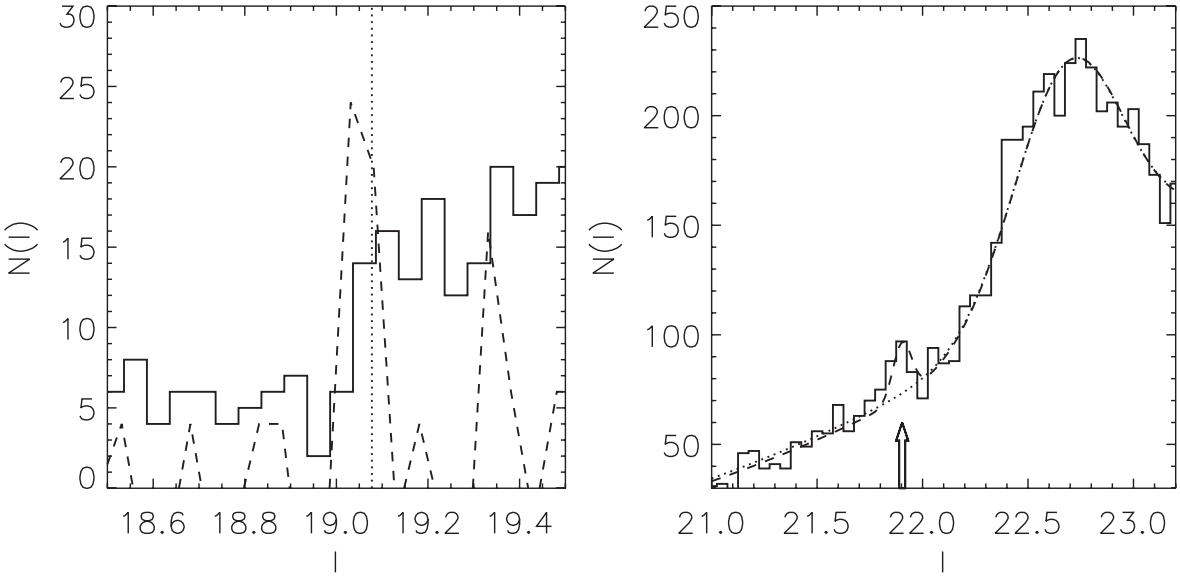

Figure 7. LF of Phoenix stars (solid histogram) in the magnitude range $18.5 < I < 19.5$ (left) and $21.0 < I < 23.2$ (right). Left: the vertical dotted line indicates the $I_{\rm tip,RGB}$ found over about 100 random realizations of the LF convolved with a Sobel filter of kernel [−2,0,2] over different binnings (see the text for more details); the dashed line shows one of these random realizations. Right: the arrow indicates the position of the RGB bump (see text); the dashed line shows the fit of equation (4) to the histogram, while the dotted line is the model LF excluding the Gaussian representing the RGB bump.

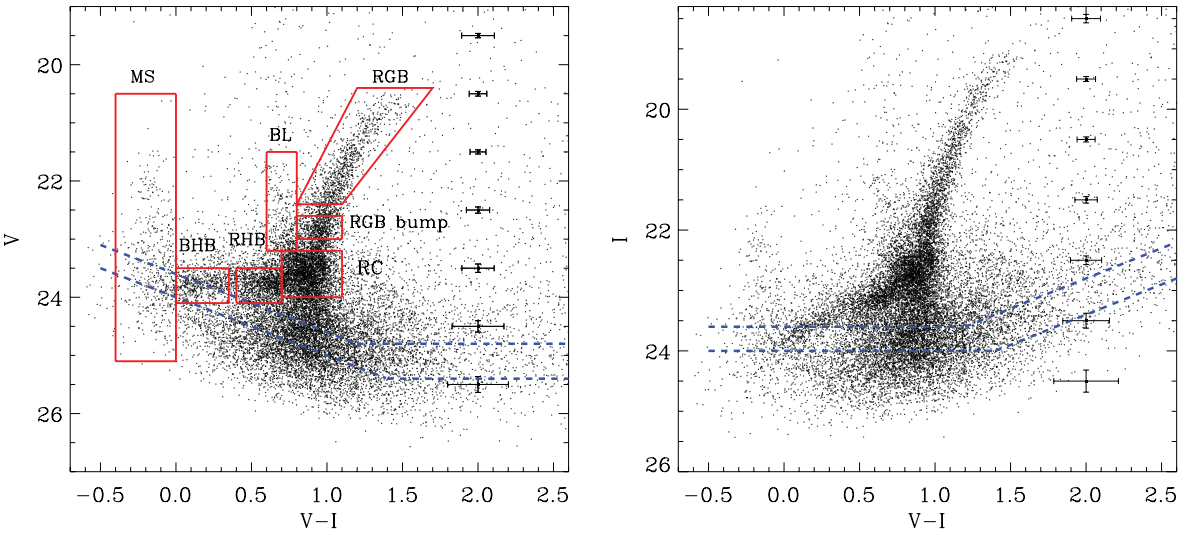

Figure 8. CMD for objects classified as stellar in the Phoenix dwarf galaxy (left: V versus $V-I$; right: I versus $V-I$). Here we do not include pointing 17, which was observed at a displaced location from the galaxy for checks on the foreground/background density. The dashed lines indicate the levels of S/N = 5 and 10 in both bands. The error bars on the right indicate the typical magnitude and colour error per magnitude bins of 0.1 mag, and they are derived from the magnitude differences of the stars with double measurements (see Fig. 3). In the left-hand panel we show the selection boxes for stars in different evolutionary phases, as indicated by the labels (see text).

We refer the reader to Holtzman et al. (2000) for a detailed discussion of the various features. Since we will use stars in different evolutionary stages to analyse how the stellar population mix varies throughout the galaxy, here we focus on how the features present in Phoenix CMD can be used as indicators of different age ranges. In evaluating the age range dominant for stars in a certain evolutionary phase, we can use the information on the Phoenix SFH and chemical enrichment history derived by H09, i.e. stars older than 6 Gyr have Z between 0.0002 and 0.0004, while the stars younger than 2 Gyr have Z between 0.001 and 0.002.

From stellar evolutionary models, it is known that HB will contain stars predominantly >10 Gyr old (ancient), while the RGB stars will sample the whole stellar population mix, with the exception of the stars younger than about 1 Gyr. The younger end of the age distribution can be explored using the BL and MS stars: the MS stars above the V_{10}, I_{10} limit, selected as in Fig. 8, are consistent with ages between 0.1 and 0.5 Gyr, while the selected BL stars are sampling slightly older stars, mainly 0.5–1 Gyr old.

The RC contains 1–10 Gyr old stars, in a proportion changing with the SFH and metallicity of the stellar population. Using the predictions on the magnitude of RC stars from Girardi & Salaris (2001), one can see that for the rather narrow and metal-poor metallicity range of stars in Phoenix, both the V and I magnitudes can act as age indicators. Therefore we split the RC stars in magnitude bins

of $V = 23.2$–23.4, 23.4–23.6 and 23.6–23.8 as indicators of age ranges 2–5, 5–8 and 8–12 Gyr, respectively. The mean magnitude of the RC (derived in Section 5.1.1) indicates that this feature is dominated by 5–8 Gyr old stars.

5.1.1 Bump on the RGB

A bump is visible along the RGB and above the RC, both in the CMDs in Fig. 8 and in the LF (see Fig. 7, right). In order to understand whether this bump can be classified as an AGB or RGB bump, we derive its mean V and I magnitudes and compare them to the predictions from stellar evolutionary models.

The I-band LF locally around the RC can be well fitted with a combination of a polynomial (for the RGB) and a Gaussian function for the RC stars (Stanek & Garnavich 1998). To this function we add another Gaussian in order to fit the bump present at brighter magnitude than the RC:

$$N(I) = a + b \times I + c \times I^2 + d \times \mathrm{e}^{-\frac{(I-I_{\mathrm{RC}})^2}{2\sigma_{\mathrm{RC}}}} + g \times \mathrm{e}^{-\frac{(I-I_{\mathrm{bump}})^2}{2\sigma_{\mathrm{bump}}}}, \quad (4)$$

where I_{RC} and I_{bump} are the mean magnitude of the RC and bump, respectively, and σ_{RC} and σ_{bump} the dispersion.

We fit equation (4) to the LF in the range $19 < I < 23.5$ in bins of 0.07 mag in a range of colour broadly covering the RC, i.e. 0.7–1.2 (see Fig. 7, right). This gives $I_{\mathrm{RC}} = 22.7$ and $\sigma_{\mathrm{I,RC}} = 0.26$ mag for the RC and $I_{\mathrm{bump}} = 21.90$, with $\sigma_{\mathrm{I,bump}} = 0.044 \pm 0.02$ mag for the bump. We also fit a similar function to the LF in V band over the same colour range and $20 < V < 24.5$; overall, such function gives a good representation of the data and yields $V_{\mathrm{RC}} = 23.54$ with a dispersion of $\sigma_{V,\mathrm{RC}} = 0.22$ mag and $V_{\mathrm{bump}} = 22.82$, with $\sigma_{\mathrm{V,bump}} = 0.13$ mag. However, since the bump feature does not seem particularly well described by a Gaussian in the V band, we also derive the V_{bump} from the observed I_{bump} by fitting the colour distribution of the stars in the range $0.8 < V - I < 1.1$ with a Gaussian. This yields a $(V-I)_{\mathrm{bump}} = 0.95$, resulting in $V_{\mathrm{bump}} = 22.85$, in good agreement with our other determination.

Using the distance modulus, the extinction and reddening values in Table 1, these would result in absolute magnitudes $M_{V,\mathrm{RC}} = +0.43$, $M_{I,\mathrm{RC}} = -0.38$, $M_{V,\mathrm{bump}} = -0.26$ and $M_{I,\mathrm{bump}} = -1.18$. The dereddened colour is $(V-I)_{\mathrm{bump},0} = 0.92$.

We examine the predicted dependency of the RGB and AGB bump magnitude and colour as a function of age and metallicity, over the range $1 \leq$ age (Gyr) ≤ 12 and $0.0001 \leq Z \leq 0.02$, in Fig. A1 (top and bottom panels, respectively). For this, we use Padua isochrones (Girardi et al. 2000; Marigo et al. 2008), in which the onset and end of the various stellar evolutionary phases are conveniently indicated.[9] We remind the reader that the SFH and chemical enrichment history derived by H09 for Phoenix show that the stars older than 6 Gyr have Z between 0.0002 and 0.0004, while the stars younger than 2 Gyr have Z between 0.001 and 0.002. Using these isochrones, we find that the magnitudes of the detected feature are not compatible with those of an AGB bump for the range of metallicities of stars in Phoenix and are instead fully compatible with the magnitudes and colour of an RGB bump for stars with metallicity Z between 0.001 and 0.0001 (see Fig. A1).

Since the work of H09 was carried out using BaSTI isochrones (Pietrinferni et al. 2004, 2006) and given that different sets of isochrones do not always predict similar magnitudes/colours for stars in the same evolutionary phase (e.g. Gallart, Zoccali & Aparicio 2005), we verified if the same conclusion would be reached using BaSTI isochrones. In this case, there is still very good agreement between the observed bump magnitudes and colours and those predicted for an RGB bump in the metallicity range appropriate for Phoenix stars, but there is also a marginal consistency with the values predicted for an AGB bump. We then examine the LFs derived for single stellar populations of ages 3, 5, 8 and 10 Gyr and $Z = 0.0001$, 0.001 and 0.01 using the online tool on the BaSTI website, and we see that the RGB bump is always more populated than the AGB bump for the metallicities of Phoenix stars. Since in our data we are able to detect only one such clump, this is most likely to be the most populated of the two, i.e. the RGB bump. Overall, then, the two sets of isochrones provide the same conclusion.

The RGB bump stars sample the intermediate and old age populations. For the same age and metallicities the AGB bump is expected at a similar colour, but about 0.5 mag brighter in the V band than the RGB bump; within our data set, however, we do not detect any evident feature at that magnitude.

RGB bumps have been detected in many LG dwarf galaxies, both in dSphs, dIrrs and dTs (see Monelli et al. 2010, and references therein); this is the first detection of the RGB bump in the Phoenix dwarf galaxy.

5.2 Spatial distribution of stellar populations

A view of how the stellar population mix changes across the galaxy can already be gleaned by examining the CMD at different distances from the centre. In Fig. 9 we plot CMDs in bins of projected elliptical radius: $R < 2$ arcmin, $2 < R < 4$ arcmin, $4 < R < 10$ arcmin. These CMDs are normalized to have the same number of stars, specifically the number of stars above the V_5, I_5 limit of the least populated spatial bin ($4 < R < 10$ arcmin). For comparison, the CMD at $R > 10$ arcmin in the figure shows where the foreground stars and unresolved background galaxies should be located. The young MS and BL stars practically disappear at $R < 4$ arcmin; the HB (>10 Gyr old) becomes much more enhanced going from the inner to the outer parts, and the RC becomes less extended in magnitude, indicating a decrease in the age range of stars in the stellar population mix; the latter is also confirmed by the tendency of the mean magnitude of RC stars in the various distance bins to become fainter at larger distances from the centre, i.e. $I_{\mathrm{RC}} = 22.65$, 22.75 and 22.86 and $V_{\mathrm{RC}} = 23.49$, 23.60 and 23.53 for $R < 2$ arcmin, $2 < R < 4$ arcmin, $4 < R < 10$ arcmin, respectively.

Fig. 10 shows the spatial distribution of stars sampling the different age ranges described in Section 5.1, i.e. MS, BL and RC in bins of V magnitude 23.2–23.4 (RC1), 23.4–23.6 (RC2), 23.6–23.8 (RC3) and RHB stars.[10] We carried out a decontamination from foreground stars and background galaxies in each of these plots by calculating the predicted number of contaminants on the area of the mosaic. This was done by using the contaminant density derived from method (a) applied to all these individual stellar populations, except for the MS stars to which we applied method (b) because of their asymmetric distribution which is clearly different from the rest of the population (see the figure). In practice, the number of contaminants was randomly removed from the objects falling in a

[9] http://stev.oapd.inaf.it/cgi-bin/cmd webpage

[10] We plot RHB stars rather than BHB stars because the latter are in smaller number and the selection box may suffer from contamination from the young MS stars.

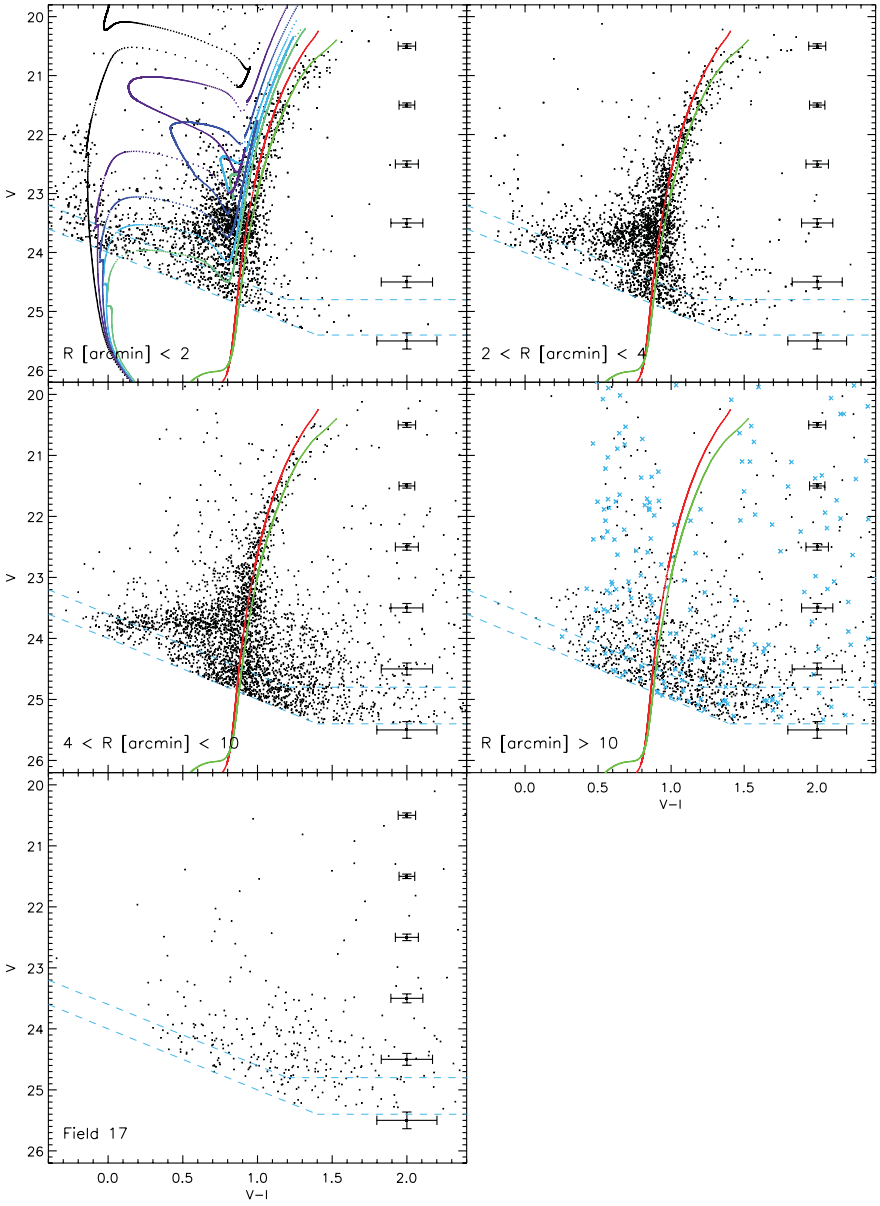

Figure 9. CMD for the objects classified as stellar in the Phoenix dwarf galaxy at different elliptical projected radii, $R < 2$ arcmin, $2 < R < 4$ arcmin, $4 < R < 10$ arcmin, $R > 10$ arcmin and in the pointing displaced from the region of the mosaic (see labels). To allow for a meaningful comparison of the relative strength of the various features in the CMD, the number of stars in the first three panels is normalized, so that they contain the same number of stars above the S/N = 5 magnitude limit. In the last two panels, whose purpose is only to show where the foreground stars and unresolved galaxies are located on the CMD, we do not apply any normalization and show all the stars present. The dashed lines indicates the S/N = 5 and 10 limits. The squares with error bars indicate the typical magnitude and colour error per magnitude bins of 0.1 mag. BaSTI isochrones (Pietrinferni et al. 2006) are overlaid on the CMD (red: 12 Gyr, α-enhanced, $Z = 3 \times 10^{-4}$; blue: 8 Gyr, solar-α, $Z = 6 \times 10^{-4}$; the other isochrones have $Z = 1 \times 10^{-3}$ and ages = 0.1, 0.3, 0.5, 0.7 and 1.0 Gyr from left to right). The crosses on the panel $R > 10$ arcmin show the location and the amount of MW foreground stars as predicted by the Besançon model (Robin et al. 2003) on to the line of sight of Phoenix over an area corresponding to the elliptical annuli $10 < R < 13$ arcmin, convolved with the observational errors in magnitude and colour; the remaining objects show the location occupied by unresolved background galaxies within the observed CMDs.

specific selection box, taking care of the fact that the density of contaminants is mostly expected to be uniform over such a small area.

It is directly visible from Fig. 10 that the younger the stellar population is, the more centrally concentrated is its spatial distribution. This is particularly evident for the youngest stars, the MS and the BL, which also show a less extended distribution with respect to the rest. This would be consistent with the star formation region shrinking with time, with recent star formation having occurred in the innermost regions where the gas density would have still been high enough to sustain it (see also H09).

Such spatial variations of the stellar population mix had also been observed in previous studies using shallower and/or less spatially extended data (e.g. Held et al. 1999; MD99; H09). The depth and spatial extent of our data allow us to perform a more accurate analysis than previous studies and quantify the variations in the spatial distribution of stars by deriving a surface number density profile for each population covering a different evolutionary stage (except

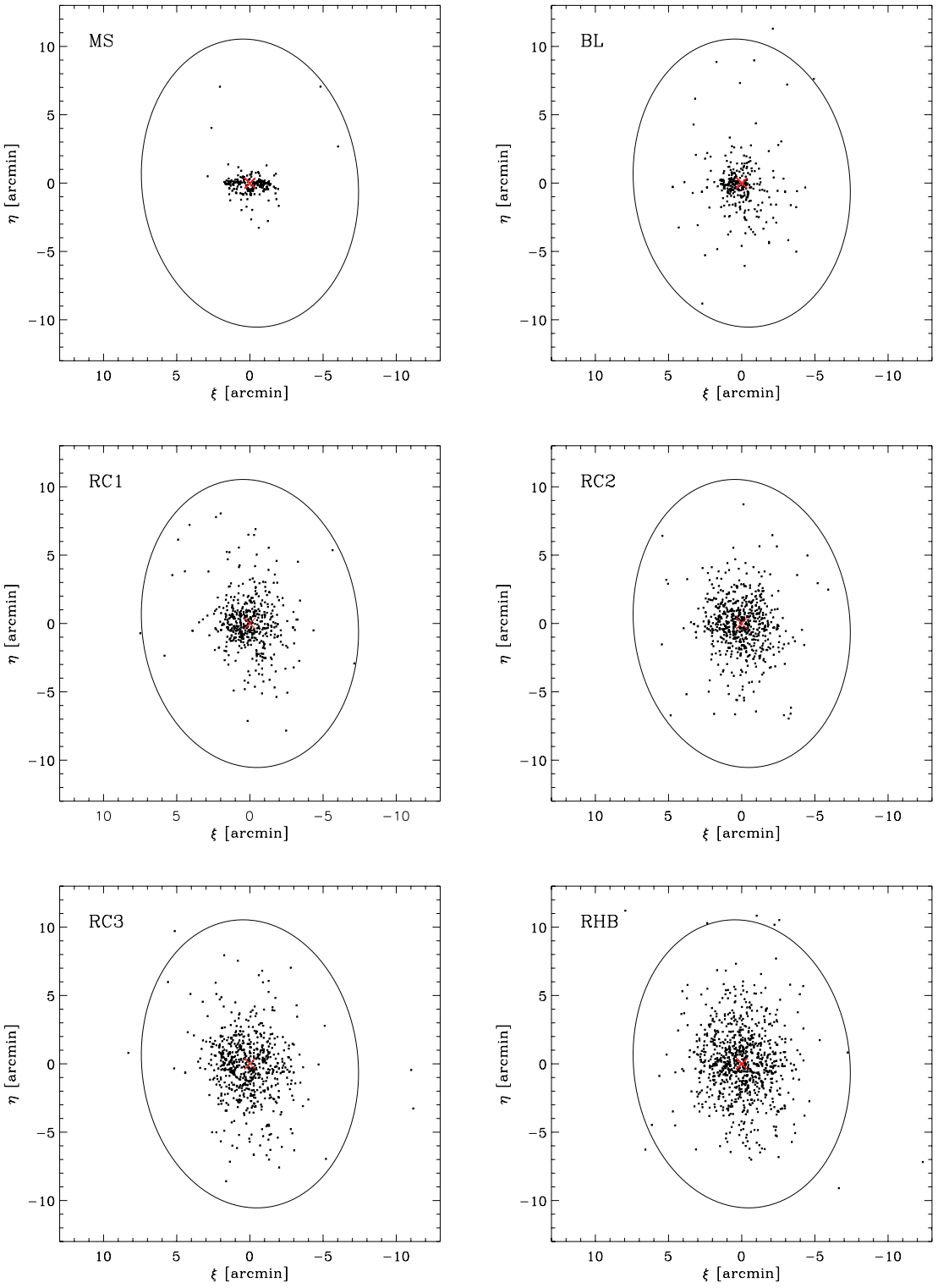

Figure 10. Spatial distribution of stars in different evolutionary stages and age ranges in the Phoenix dwarf galaxy, i.e. MS, BL, RC in bins of V magnitude 23.2–23.4 (RC1), 23.4–23.6 (RC2), 23.6–23.8 (RC3) and RHB stars as indicated by the labels and boxes in Fig. 8. The various populations have been extracted from the S/N > 10 sample. A decontamination has been carried out, using the contaminant density derived as a weighted mean of the outer points of the surface density profile (except for the MS stars for which we used the contaminant density derived from the objects at $R > 12.6$ arcmin). The ellipse shows the measurement of the nominal tidal radius derived in this work. A red cross is placed at the coordinates of Phoenix optical centre to guide the eye. North is up and East is on the left.

for the flattened, asymmetric MS stars). The methodology and the functional forms fitted to the observed profiles are as described in Section 3.2. The best-fitting parameters (see Table 7) show that the variations among the spatial distribution of the various stellar populations appear smooth, slowly and steadily going from more concentrated distributions for the youngest populations to more extended distributions for the oldest populations. We checked that using the contaminant density derived from method (b) to all stellar populations would bring negligible changes to the resulting spatial distributions, surface brightness profiles and the resulting best-fitting parameters [as in the case of the overall stellar population, the reduced χ^2 values of the best-fitting profiles are larger when using method (b) than method (a)]. Also, the determination of the outer points over which we calculate the density of contaminants was adjusted by identifying where the surface number profile was becoming approximately flat; we checked that the choice of this region did not influence the results.

As noted in previous works (e.g. MD99), the MS stars, those approximately younger than 0.7 Gyr, have a flattened distribution, almost perpendicular to the other stellar components. There appears to be two main clumps of young MS stars. Some clumping is also present in the distribution of the other young stars, i.e., the BL and the RC1 that represent the stars with ages mostly between 2 and 5 Gyr, both of which show a rather spherical concentration of stars displaced from the centre, towards the south-east at rectangular coordinates (+0.5,−0.5); this is the direction of the coordinates we find for the position of the centre in the inner 2 arcmin in Fig. 5. Such displaced concentration disappears when moving to older ages, where the distribution becomes more regular. It can be noted that the populations on average older than 2 Gyr have a regular, spheroidal appearance and do not display a disc-like distribution as the young MS stars. Therefore the overall configuration of Phoenix does not resemble a disc–halo structure like larger spiral galaxies such as the MW: in the MW the disc contains stars of all ages (from young to ancient), while the halo is formed solely of ancient stars; this is different from the situation in Phoenix, where the disc-like feature is composed only of young stars, while the spheroidal part of the galaxy contains stars from intermediate to ancient ages.

We can speculate that the flattened, asymmetric distribution of the young MS stars still retains the imprint of where the recent star formation took place, and therefore of where the gas was recently located. This appears also to be still imprinted in the distribution of slightly older stars, such as the BL and the RC1, in the form of the clump displaced from the centre. However, being slightly older than the MS, these BL and RC1 stars would have had more time to become sensitive to the overall potential of the galaxy, and for their spatial distribution to become smoother.

6 DISCUSSION

6.1 Spatial variations of the stellar population mix

The spatial distribution of the stars changes with radius and becomes less and less centrally concentrated the older the stellar population. This is reflected in the values of the best-fitting parameters of the surface number profiles of the different stellar populations that steadily go from a more concentrated to less concentrated distribution with increasing ages.

Similar variations in the stellar population mix appear to be a common characteristic of LG dwarf galaxies (see e.g. Harbeck et al. 2001; Tolstoy et al. 2004; Battaglia et al. 2006; Bernard et al. 2008; Monelli et al. 2012), with the star formation proceeding longer in the central regions. There are a number of mechanisms that could cause this: a natural evolution of the gas, for example, progressively sinking in the centre in the absence of rotation (e.g. Stinson et al. 2009; Schroyen et al. 2011) or reaching higher densities in the centre and therefore continuing star formation for longer. Other explanations could be ejection of the interstellar medium because of supernova explosions being more efficient in the outer parts and removal of the gas from ram pressure/tidal stripping (e.g. Mayer et al. 2006).

Stinson et al. (2009) show that age gradients of this type can arise in model isolated galaxies of low mass (with virial velocities $\lesssim$20 km s^{-1}) without any need for external factors, because these systems do not form stable star-forming discs, as the gas is mostly supported by pressure rather than angular momentum. Star formation rate (SFR) is initially high in the centre, because of the larger densities of the gas, and while the gas is consumed, the disc contracts until pressure support is re-established. Further shrinking may be due to a lower turbulence velocity due to the decline in SFR in the centre, which maintains high gas densities in the centre but not in the outer regions, resulting in a star formation that is systematically less radially extended as time goes on.

It appears that whatever the mechanism is that creates evident variations in the stellar population mix, it can act on very different time-scales from galaxy to galaxy. The Sculptor dSph, which predominantly consists of stars older than 10 Gyr (e.g. de Boer et al. 2012), clearly displays this feature already in its ancient population (Tolstoy et al. 2004; de Boer et al. 2012). In the Fornax dSph instead there is no detected spatial variation in the mix of the ancient population, while these changes are clear when comparing ancient, intermediate age and young stars (e.g. Stetson, Hesser & Smecker-Hane 1998; Battaglia et al. 2006). Phoenix in this respect is similar to Fornax. Such spatial variations between populations of different ages could be expected if they are due to environmental effects: more isolated objects and satellites with less internal/eccentric orbits around the host galaxy would be less affected and star formation could proceed longer in the outer parts; this would be consistent with what is presently known about the orbits of Sculptor and Fornax, bar the large error bars in the proper motions values. At present there are no determinations of the proper motion of Phoenix; assuming a radial orbit for this object, its systemic velocity (e.g. Irwin & Tolstoy 2002) referred to as the Galactic rest frame ($v_{\rm sys,GSR} \sim -100$ km s^{-1}) would yield an $r \times v^2$ about 1.5 times lower than that for Leo I, which is considered as a satellite of the MW: in principle, Phoenix could therefore still be a MW satellite falling back.

In order to disentangle environmental effects from internal ones, it would be instructive to quantify the differences in the distribution of stellar populations of various ages in a sample of LG dwarf galaxies. The isolated objects would give insights into the extent to which internal mechanisms can be responsible for the variations in the stellar population mix. It would be also instructive to compare systems with similar SFHs: for example, Sculptor, Tucana and Cetus are all dSphs which produced most of their stars very early on, but while the former is a MW satellite, the other two are found far from the MW and M31. There are indications that also among the ancient stars in Tucana and Cetus, the older/metal-poor ones have a more extended spatial distribution than the younger/metal-rich ones (Harbeck et al. 2001; Bernard et al. 2008; Monelli et al. 2012); it remains to be quantified how these differences in the distribution of the ancient stars compare between isolated and non-isolated dwarf galaxies.

6.2 Spatial distribution of young stars

The stars younger than 0.7 Gyr display a clearly different spatial distribution from the rest of the population: not only do they virtually disappear at distances larger than 4 arcmin from the centre, but they are almost perpendicular to the bulk of the other stars, and the distribution is asymmetric and more flattened. This was already noted by VDK91 and MD99. By separating the sample in age bins, we also see that some asymmetries in the form of clumps are visible in the spatial distribution of BL stars and the younger RC stars, while stars older than about 5 Gyr display regular spatial distributions.

We can speculate that the flattened, asymmetric distribution of the young MS stars still retains the imprint of where recent star formation took place, and therefore of where the gas was recently located. This appears also to be still imprinted in the distribution of the BL and young RC stars; however, since these stars are older than the young MS stars, they have had more time to diffuse to larger distance and to become more sensitive to the overall potential of the galaxy, resulting in a smoother distribution. Following this reasoning, it is likely that in a few hundred Myr the young MS stars also will diffuse to larger distances and acquire a more regular morphology, similar to the one of the main body of the galaxy. At that stage, Phoenix would probably look like a typical dSph, if it also were to lose its H I gas or exhaust it in further star formation.

In the models of Stinson et al. (2009) for low-mass objects, although the majority of stars form systematically more inwards the more time passes, some amount of radial migration is also present, which goes in the direction of pushing stars to larger radii with respect to their birth site, qualitatively consistent with what we see here for the youngest stars.

We point out that a feature such as the one seen here – an inner flattened component containing young stars and tilted with respect to the main body of the galaxy – is also present in other LG dwarfs such as the Leo A dIrr (e.g. see fig. 1 in Cole et al. 2007) and the closer by Fornax dSph, a MW satellite. With respect to the majority of MW dSphs, Fornax has had a much more extended SFH and is the only one to show stars possibly as young as 50 Myr (Coleman & de Jong 2008). Also, in this galaxy the young MS stars show a flattened distribution, tilted with respect to the main stellar population, while the slightly older BL stars have a less asymmetric and flattened distribution and appear to have diffused to larger distances. In this case, the tilting of the young stars is less enhanced, being approximately 40° (e.g. Stetson et al. 1998).

It is unclear what would cause the tilting of the youngest stars with respect to the bulk of the stellar population. Such a behaviour has not been reported for more massive, clearly rotating systems, such as for example the Wolf–Lundmark–Melotte (WLM) dIrr (Leaman et al. 2012), where the young stars would be aligned and concentric with the distribution of older stars and the gas. This may indicate an influence of the total mass of the galaxy in determining its intrinsic angular momentum, and consequently the resulting distribution of its stellar populations: we speculate that, in less massive systems, the low amount of angular momentum would permit a disordered configuration of the gas, and therefore of the stars young enough not to have become sensitive to the overall potential of the galaxy. In apparent contradiction to that, in NGC 6822, a dIrr with a luminosity similar to WLM, the spatial distributions of the young stars and the old RGB stars are almost perpendicular to each other, with the young stars following the H I disc (e.g. Demers, Battinelli & Kunkel 2006); in this case, however, the picture is complicated by the complex disc structure (Cannon et al. 2012) and the classification of NGC 6822 as a polar ring galaxy (e.g. Demers et al. 2006).

6.3 Disc–halo appearance

Previous works (e.g. MD99) showed that the central parts of Phoenix display an inner component that is tilted with respect to the main body of the galaxy and that morphologically resembles a disc – while the main body has a spheroidal distribution. The question was raised whether Phoenix may have a disc–halo structure similar to that of large spirals galaxies, such as the MW.

We can comment on this issue simply making some consideration on the age of the stars found in the 'disc' and the 'halo' of Phoenix.

In this work we showed that in Phoenix only young stars are responsible for the elongated central structure that morphologically resembles a disc, while such structure is absent for stars older than 2 Gyr, which display a rather regular spheroidal morphology. Therefore only stars younger than 1 Gyr are found in the 'disc', while both intermediate age and ancient stars are found in the 'halo'. This is clearly different from what is observed for the MW, where the disc is known to contain stars of all ages, while the halo consists of ancient stars; therefore the structure we see in Phoenix is not analogous to what was found in the MW and M31.

This result is also difficult to reconcile with the properties of stellar haloes formed in a Λ cold dark matter (ΛCDM) context. Stellar haloes formed from disrupted satellite galaxies are a natural consequence of the hierarchical formation of galaxies in a ΛCDM framework and, for large spirals, the average age of stars in the stellar haloes is expected to be around 11 Gyr (Cooper et al. 2010), with essentially no stars younger than 5 Gyr, from mainly a few satellites accreted between redshifts 1 and 3. Since in this context dwarf galaxies are expected to be among the first galactic systems to form, their stellar haloes should arguably have formed at earlier times than for large spirals, and from smaller progenitors, and should therefore contain only ancient stars.

7 SUMMARY AND CONCLUSIONS

We presented results from wide-area photometry in V and I band from VLT/FORS for Phoenix, one of the few transition-type dwarf galaxies of the LG. The data consist of a mosaic of images covering 26×26 arcmin^2 around the optical centre of the galaxy and reaching below the HB of the system: this is the only data set for this galaxy that combines relatively deep photometry with such a large spatial coverage. For comparison with previous studies, we can trace Phoenix stellar population out to projected radii of 1.5 kpc from its centre, while the study of H09 reached out to 0.5 kpc.

One output of the analysis is the redetermination of the overall structure of the system and especially its extent, whose value was very uncertain in the literature. We derived a nominal tidal radius of $r_t = 10.56 \pm 0.15$ arcmin, about 60 per cent the value determined by MD99. The best-fitting profile to the overall stellar population of Phoenix is a Sérsic profile of Sérsic radius $R_S = 1.82 \pm 0.06$ arcmin and $m = 0.83 \pm 0.03$.

The distance of Phoenix has been derived independently from our data set using the RGB tip method, and it is in agreement with previous distance determinations from H09 and M99. Examination of the CMD and LF revealed the presence of a bump above the RC, consistent with being a RGB bump. This is the first detection of this feature in Phoenix.

The depth of the photometry allows us to study stars in different evolutionary phases, with ages ranging from about 0.1 Gyr to the oldest ages as they can be identified from features in the CMD. This, combined to the large area covered, enabled us to explore in

a very direct way how the stellar population mix varies across the face of the galaxy.

The spatial distribution of the stars changes with radius and becomes less and less centrally concentrated the older the stellar population. This is reflected in the values of the best-fitting parameters of the surface number profiles of the different stellar populations that we provide.

As also found in previous studies, Phoenix displays in the inner regions a flattened structure, almost perpendicular to the main body of the galaxy. This feature was suggestive of a disc–halo structure and was raising the question whether Phoenix also could consist of a disc–halo system such as the one found in the MW. We showed that the flattened, tilted structure appears to be present mainly among stars younger than 1 Gyr, and absent for the stars $\gtrsim$5 Gyr old, which on the other hand show a regular distribution also in the centre of the galaxy. This argues against a disc–halo structure of the type found in large spirals such as the MW.

ACKNOWLEDGMENTS

The research leading to these results has received funding from the European Union Seventh Framework Programme (FP7/2007-2013) under grant agreement number PIEF-GA-2010-274151. We acknowledge the International Space Science Institute (ISSI) at Bern for their funding of the team 'Defining the full life-cycle of dwarf galaxy evolution: the Local Universe as a template'. This work has made use of BaSTI web tools provided at www.oa-teramo.inaf.it/BASTI. We acknowledge the use of the online catalogues for standard stars provided by P. Stetson at http://www3.cadc-ccda.hia-iha.nrc-cnrc.gc.ca/community/STETSON/standards/. GB thanks Michele Cignoni and Francesca Annibali for useful suggestions.

REFERENCES

Akaike H., 1973, in Petrov B. N., Csaki F. eds, Second Int. Symp. Information Theory, Information Theory and an Extension of the Maximum Likelihood Principle. Akademiai Kiado, Budapest, p. 267
Appenzeller I., Rupprecht G., 1992, Messenger, 67, 18
Battaglia G. et al., 2006, A&A, 459, 423
Battaglia G., Helmi A., Tolstoy E., Irwin M., Hill V., Jablonka P., 2008, ApJ, 681, L13
Bellazzini M., Gennari N., Ferraro F. R., Sollima A., 2004, MNRAS, 354, 708
Bellazzini M. et al., 2011, A&A, 527, A58
Bernard E. J. et al., 2008, ApJ, 678, L21
Caldwell N., 1999, AJ, 118, 1230
Cannon J. M. et al., 2012, ApJ, in press (arXiv:1201.3149)
Caon N., Capaccioli M., D'Onofrio M., 1993, MNRAS, 265, 1013
Cardelli J. A., Clayton G. C., Mathis J. S., 1989, ApJ, 345, 245
Cole A. A. et al., 2007, ApJ, 659, L17
Coleman M. G., de Jong J. T. A., 2008, ApJ, 685, 933
Coleman M. G., Da Costa G. S., Bland-Hawthorn J., Freeman K. C., 2005a, AJ, 129, 1443
Coleman M. G., Da Costa G. S., Bland-Hawthorn J., 2005b, AJ, 130, 1065
Cooper A. P. et al., 2010, MNRAS, 406, 744
Da Costa G. S., Armandroff T. E., 1990, AJ, 100, 162
de Boer T. J. L. et al., 2012, A&A, 539, A103
Demers S., Battinelli P., Kunkel W. E., 2006, ApJ, 636, L85
Freudling W., Romaniello M., Patat F., Møller P., Jehin E., O'Brien K., 2007, in Sterken C., ed., ASP Conf. Ser. Vol. 364, The Future of Photometric, Spectrophotometric and Polarimetric Standardization. Astron. Soc. Pac. San Francisco, p. 113
Gallart C., Martínez-Delgado D., Gómez-Flechoso M. A., Mateo M., 2001, AJ, 121, 2572
Gallart C., Aparicio A., Freedman W. L., Madore B. F., Martínez-Delgado D., Stetson P. B., 2004, AJ, 127, 1486
Gallart C., Zoccali M., Aparicio A., 2005, ARA&A, 43, 387
Girardi L., Salaris M., 2001, MNRAS, 323, 109
Girardi L., Bressan A., Bertelli G., Chiosi C., 2000, A&AS, 141, 371
Graham A. W., Guzmán R., 2003, AJ, 125, 2936
Harbeck D. et al., 2001, AJ, 122, 3092
Held E. V., Saviane I., Momany Y., 1999, A&A, 345, 747
Hidalgo S. L., Aparicio A., Martínez-Delgado D., Gallart C., 2009, ApJ, 705, 704 (H09)
Holtzman J. A., Smith G. H., Grillmair C., 2000, AJ, 120, 3060
Irwin M., Hatzidimitriou D., 1995, MNRAS, 277, 1354
Irwin M., Tolstoy E., 2002, MNRAS, 336, 643
Jerjen H., Rejkuba M., 2001, A&A, 371, 487
Karachentsev I. D., Karachentseva V. E., Huchtmeier W. K., Makarov D. I., 2004, AJ, 127, 2031
Kazantzidis S., Łokas E. L., Callegari S., Mayer L., Moustakas L. A., 2011, ApJ, 726, 98
King I., 1962, AJ, 67, 471
Leaman R. et al., 2012, ApJ, 750, 33
Lee M. G., Freedman W. L., Madore B. F., 1993, ApJ, 417, 553
Majewski S. R. et al., 2005, AJ, 130, 2677
Marigo P., Girardi L., Bressan A., Groenewegen M. A. T., Silva L., Granato G. L., 2008, A&A, 482, 883
Martínez-Delgado D., Gallart C., Aparicio A., 1999, AJ, 118, 862 (MD99)
Martínez-Delgado D., Alonso-García J., Aparicio A., Gómez-Flechoso M. A., 2001, ApJ, 549, L63
Mateo M. L., 1998, ARA&A, 36, 435
Mayer L., Mastropietro C., Wadsley J., Stadel J., Moore B., 2006, MNRAS, 369, 1021
Menzies J., Feast M., Whitelock P., Olivier E., Matsunaga N., da Costa G., 2008, MNRAS, 385, 1045
Monelli M., Cassisi S., Bernard E. J., Hidalgo S. L., Aparicio A., Gallart C., Skillman E. D., 2010, ApJ, 718, 707
Monelli M. et al., 2012, MNRAS, submitted (arXiv:1201.2821)
Pietrinferni A., Cassisi S., Salaris M., Castelli F., 2004, ApJ, 612, 168
Pietrinferni A., Cassisi S., Salaris M., Castelli F., 2006, ApJ, 642, 797
Plummer H. C., 1911, MNRAS, 71, 460
Robin A. C., Reylé C., Derrière S., Picaud S., 2003, A&A, 409, 523
Salaris M., Chieffi A., Straniero O., 1993, ApJ, 414, 580
Schlegel D. J., Finkbeiner D. P., Davis M., 1998, ApJ, 500, 525
Schroyen J., de Rijcke S., Valcke S., Cloet-Osselaer A., Dejonghe H., 2011, MNRAS, 416, 601
Sersic J. L., 1968, Atlas de Galaxias Australes. Observatorio Astronomico, Cordoba, Argentina
Stanek K. Z., Garnavich P. M., 1998, ApJ, 503, L131
Stetson P. B., 1987, PASP, 99, 191
Stetson P. B., 2000, PASP, 112, 925
Stetson P. B., Hesser J. E., Smecker-Hane T. A., 1998, PASP, 110, 533
Stinson G. S., Dalcanton J. J., Quinn T., Gogarten S. M., Kaufmann T., Wadsley J., 2009, MNRAS, 395, 1455
Tolstoy E. et al., 2004, 617, L119
Tolstoy E., Hill V., Tosi M., 2009, ARA&A, 47, 371
Trujillo I., Erwin P., Asensio Ramos A., Graham A. W., 2004, AJ, 127, 1917
van de Rydt F., Demers S., Kunkel W. E., 1991, AJ, 102, 130 (VDK91)
Wilkinson M. I., Kleyna J. T., Evans N. W., Gilmore G. F., Irwin M. J., Grebel E. K., 2004, ApJ, 611, L21
Young L. M., Skillman E. D., Weisz D. R., Dolphin A. E., 2007, ApJ, 659, 331

APPENDIX A: RGB AND AGB BUMP

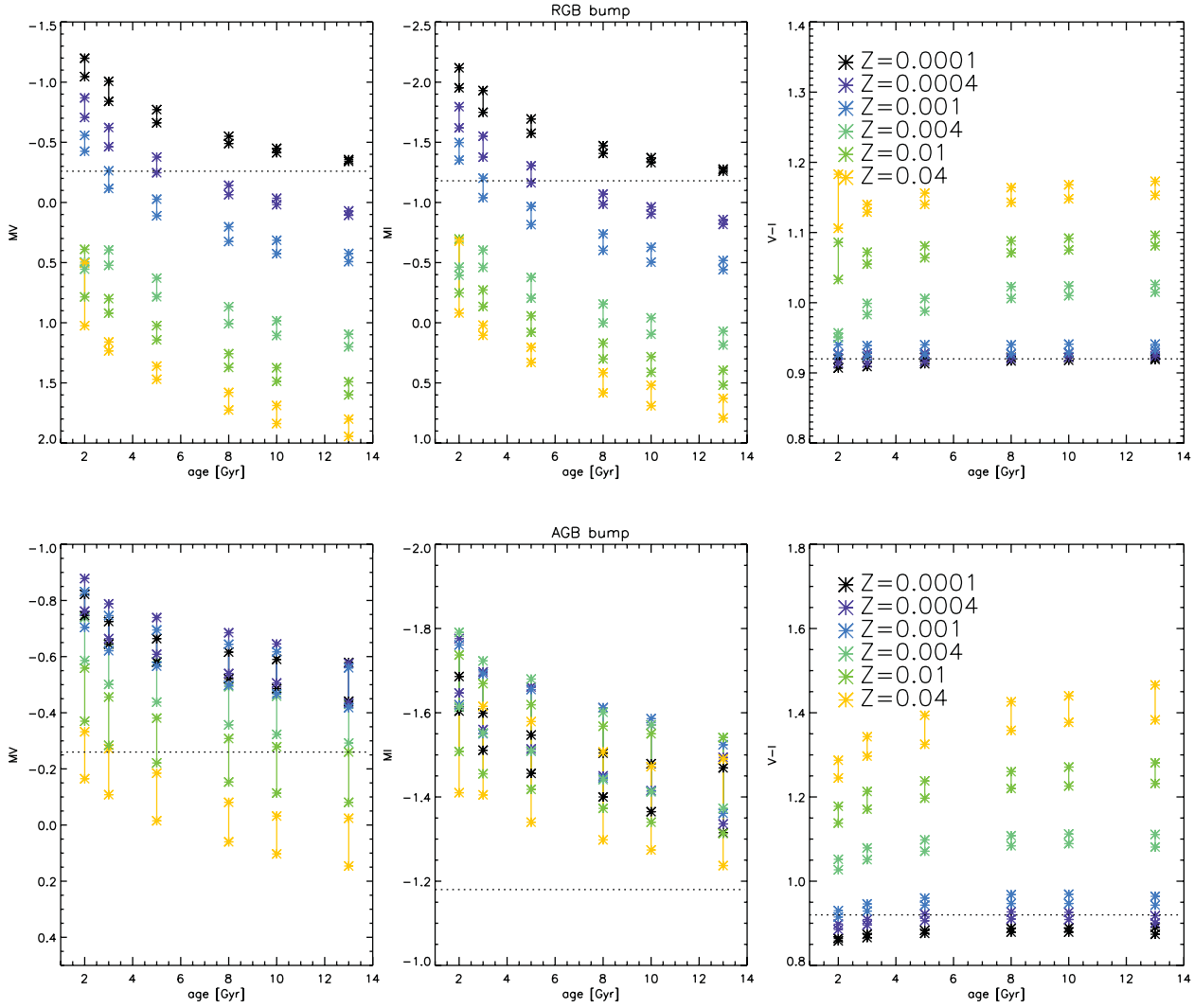

Figure A1. For this figure we used solar-scaled Padua isochrones (Marigo et al. 2008) spanning an age range from 2 to 13 Gyr and $Z = 0.0001$–0.02. Top: the symbols connected by vertical lines show the luminosity interval of RGB stars crossing the discontinuity in chemical profile left by the first dredge-up event. This interval corresponds to the bump in the LF along the RGB. Bottom: as before, but this interval corresponds to the clump of early AGB stars in CMDs and therefore the AGB bump. From left to right we show how the V magnitude, I magnitude and $V - I$ colour vary as a function of age in Gyr for isochrones of different metallicities.

SUPPORTING INFORMATION

Additional Supporting Information may be found in the online version of this article:

Table 5. Catalogue of bona fide stars from FORS photometry of the Phoenix dT, including pointing 17.

Please note: Wiley-Blackwell are not responsible for the content or functionality of any supporting materials supplied by the authors. Any queries (other than missing material) should be directed to the corresponding author for the article.

This paper has been typeset from a TEX/LATEX file prepared by the author.